Eigenmode analysis of membrane stability in inviscid flow

Christiana Mavroyiakoumou[*] and Silas Alben[†]

Department of Mathematics, University of Michigan, Ann Arbor, Michigan 48109, USA

We study the instability of a thin membrane (of zero bending rigidity) to out-of-plane deflections, when the membrane is immersed in an inviscid fluid flow and sheds a trailing vortex-sheet wake. We solve the nonlinear eigenvalue problem iteratively with large ensembles of initial guesses for three canonical boundary conditions—both ends fixed, one end fixed and one free, and both free. Over several orders of magnitude of membrane mass density, we find instability by divergence or flutter (particularly at large mass density or with one or both ends free). The most unstable eigenmodes generally become wavier at smaller mass density and smaller tension but with regions of nonmonotonic behavior. We find good quantitative agreement with unsteady time-stepping simulations at small amplitudes, but only qualitative similarities with the eventual steady-state large-amplitude motions.

I. INTRODUCTION

When extensible membranes of zero bending rigidity are placed in a fluid flow, the interaction between membrane inertia, resistance to stretching, and external fluid forces can result in complex time-dependent deformations and dynamics. This holds both for large-amplitude motions and the initial small-amplitude motions that determine the stability of undeflected membranes. Predicting the onset of membrane instability across parameter space, either by flutter, divergence, or a combination of the two [1–3], is fundamental to a wide range of applications. As lightweight, deployable structures that are stable in a variety of configurations, membranes are used, for example, in sails [4–8], parachutes [9,10], micro-air vehicles [11–15], ballutes for space exploration [16,17], supersonic aircraft and rockets [18–20], roofs in civil engineering [2,21–23], and the wings of flying animals [24–26].

In an early work, Nielsen [8] studied a membrane with both edges fixed in a two-dimensional flow and determined the critical value of the pretension parameter that gives rise to a fully convex membrane shape. An overview of early models based on potential-flow aerodynamics can be found in Ref. [6]. Previous works have studied the difference between the flutter of membranes (with zero bending rigidity) and plates in the limit of zero bending rigidity. Because the bending rigidity term has the highest (fourth-order) spatial derivative, it is a singular limit and thus the two problems can have significant differences. In the case of panels in supersonic flows, the membrane is stable whereas the plate can be unstable to flutter in the limit [27–29]; see also Ref. [[30], pp. 25–26]. This so-called membrane paradox also arises in solar sails [31] and a related boundary-layer phenomenon occurs for heaving plates, hanging under gravity [32]. Over the past few decades, theoretical [2,33], computational [1,3,34,35], and experimental [36] studies of membrane stability have revealed a wide range of membrane stability behavior and dynamics with various boundary conditions.

---

[*]chrismav@umich.edu

[†]alben@umich.edu

In Ref. [1], we used a nonlinear time-stepping algorithm to compute the stability thresholds for membranes with three sets of boundary conditions: fixed-fixed, fixed-free, and free-free leading and trailing edges. Membrane tension has a stabilizing effect in all cases. The ratio of membrane-to-fluid inertia has a less obvious effect—heavier membranes may be unstable when a lighter membrane was not, but the instability grows more slowly as membrane mass increases, to the point where it is difficult to determine whether the membrane is stable or not. Nonlinear time-stepping simulations with evolving vortex sheet wakes are expensive when large simulation times are required (i.e., to assess the stability of heavy membranes), and when the membrane develops fine deformations (as occurs for lighter membranes and smaller pretension values). In the latter case, a fine grid on the membrane is required, increasing the size of the coupled system of equations that is solved implicitly, and making it more ill-conditioned, slowing convergence at each time step.

Therefore, in this paper, we develop a less expensive alternative to study the stability problem—a nonlinear eigenmode solver. We solve for an ensemble of eigenmodes and corresponding eigenvalues (growth rates and frequencies) corresponding to small-amplitude deformations. By comparing with unsteady simulations, we find that the modes accurately capture the early stages of the unsteady motion starting from the undeflected state. By comparing at later times, we find that the mode shapes qualitatively resemble those of the steady-state large amplitude motions to varying degrees.

Due to the vortex wake, simple exact eigenmode solutions are difficult to obtain and the physical mechanisms that underlie the membrane instability are somewhat elusive, but in the present paper we are able to present a comprehensive characterization of the modes and growth rates in the vicinity of the stability boundary. The eigenmode approach has been used previously to study membrane stability with fixed-fixed [2,3,8,35] and periodic [33] boundary conditions. We use our method on the fixed-fixed case, as well as the fixed-free and free-free cases introduced in Ref. [1], where a wider range of dynamics can occur. In each case, we study a much wider range of membrane mass density and pretension values than previous studies. A version of the present method was previously used to study the flutter instability of bending beams in inviscid flows [37]. There solutions were obtained by continuation, starting from the known oscillation modes of a beam in a vacuum. Here we study membranes (with zero bending rigidity) and find that the continuation approach is now more susceptible to jumping between different eigenmode branches as we vary parameters. Therefore, we solve the nonlinear eigenvalue problem using dense meshes of initial eigenvalue guesses that cover the range of lower-mode states. As a result, we obtain a larger ensemble of eigenmodes at each parameter value set. We obtain good agreement with the stability results in Ref. [1] but are able to extend the results to much larger and smaller values of the membrane-to-fluid density ratio and resolve shapes with finer structures.

The structure of the paper is as follows. In Sec. II, we present the membrane and vortex sheet model and in Sec. III its linearized, small-amplitude version, along with a summary of the numerical method for determining the eigenvalues and eigenmodes (Sec. III A). In Secs. IV–VI, we present our results for an extensive range of parameters for each of the three boundary conditions. We then turn to simulations of the initial value problem and examine how the unsteady motions compare to the eigenmode shapes from the linearized model (Sec. VII). Section VIII presents conclusions.

II. MEMBRANE-VORTEX-SHEET MODEL

We model the dynamics of an extensible membrane that is nearly aligned with a two-dimensional background fluid flow with speed U in the far field (see Fig. 1).

In Fig. 1, we illustrate schematically the three cases of boundary conditions at the two ends of the membrane that we investigated in Ref. [1]: fixed-fixed [Figs. 1(a) and 1(b)], fixed-free [Figs. 1(c) and 1(d)], and free-free [Figs 1(e) and 1(f)]. In all three cases, the x coordinates of the ends are fixed at 0 and $2L$. In the fixed-fixed case, we set the deflection to zero at both ends of the membrane; most previous studies of membrane flutter considered this boundary condition [2,3,35,36,38]. In the fixed-free case, the leading edge deflection is again set to zero but the trailing edge is allowed to deflect freely in the vertical direction. This is the classical free-end boundary condition for a membrane
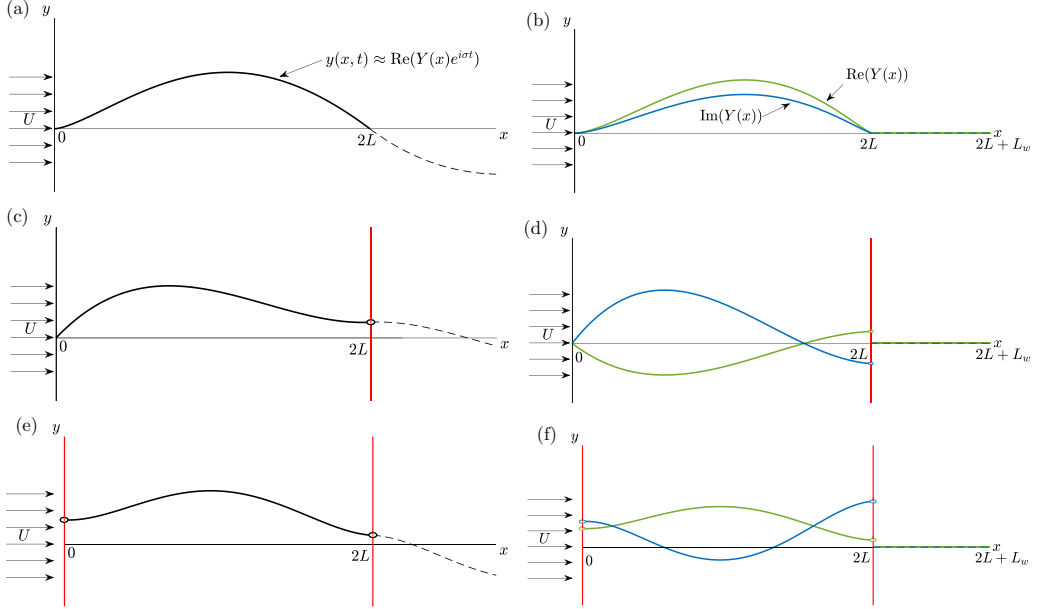
FIG. 1. Schematic diagram of flexible membranes (solid curved black lines) at an instant in time. Here $2L$ is the chord length (the distance between the endpoints) and U is the oncoming flow velocity. For the nonlinear, large-amplitude model [(a), (c), (e)], $y(x, t)$ is the membrane deflection and the dashed line is the free vortex wake. The right columns show the corresponding linearized, small-amplitude eigenvalue problems, where the motions are represented by the real and imaginary parts of the eigenmodes $Y(x)$, shown as green and blue lines, respectively, and flat vortex wakes of fixed length L_w shown as dashed lines at $y = 0$ [(b), (d), (f)]. The boundary conditions shown are: fixed-fixed membranes [(a), (b)], fixed-free membranes [(c), (d)], and free-free membranes [(e), (f)].

[39,40]. The membrane end is fixed to a massless ring that slides along a vertical frictionless pole (represented by the red lines in Fig. 1). Since the pole is frictionless and the ring is massless, the membrane can exert no vertical force on the free end by tension, and hence the membrane slope must be zero.

Free-end boundary conditions have been implemented in various problems in classical mechanics such as beam flutter [41–60], but they have not been used to a great extent in membrane flutter problems. Recently, an experimental study determined that membrane wing flutter can be enhanced by the vibrations of flexible leading and trailing edge supports [61]. For membrane wings with partially free trailing edges, trailing edge fluttering may occur at relatively low angles of attack [12]. Partially free edges also occur in sails. In Ref. [5], it is shown that by altering the tension in cables running along its free edges, one can control the shape of a sail membrane and when the tension in these edges is sufficiently low, flutter can occur [4]. A related application is energy harvesting by membranes mounted on tensegrity structures and placed in fluid flows [62,63].

The authors in Refs. [32,64] consider the dynamics and flutter of membranes and cables under gravity with free ends. In Ref. [1] and in the current paper, to focus on the basic flutter problem [65], we do not include gravity in the model. However, we still need to ensure that the problem remains well-posed by requiring some restriction on the motion of the free membrane ends to eliminate the possibility of membrane compression [64]. This restriction is provided by the vertical frictionless poles. This has been carried out experimentally by representing a membrane as an extensional spring tethered by steel wires to vertical supports [66], for example.

The model here is the same as in Ref. [1] but we repeat the main points for completeness. The membrane dynamics are described by the unsteady extensible elastica equation with body inertia,

stretching resistance, and fluid pressure loading, obtained by writing a force balance equation for a small section of membrane lying between α and $\alpha + \Delta\alpha$:

$$\rho_s hW \partial_{tt}\zeta(\alpha, t)\Delta\alpha = T(\alpha + \Delta\alpha, t)\hat{\mathbf{s}} - T(\alpha, t)\hat{\mathbf{s}} - [p]_-^+(\alpha, t)\hat{\mathbf{n}}W(s(\alpha + \Delta\alpha, t) - s(\alpha, t)). \quad (1)$$

Here ρ_s is the mass per unit volume of the undeflected membrane, h is its thickness, and W is its out-of-plane width, all uniform along the length. In Eq. (1), $\zeta(\alpha, t) = x(\alpha, t) + iy(\alpha, t)$ is the membrane position in the complex plane, parameterized by the material coordinate α, $-L \leqslant \alpha \leqslant L$ (L is half the chord length) and time t. The pressure jump across the membrane is $[p]_-^+$, the local arc length coordinate is $s(\alpha, t)$, the local stretching factor is $\partial_\alpha s$, and the unit vectors tangent and normal to the membrane are $\hat{\mathbf{s}}$ and $\hat{\mathbf{n}}$, respectively. These are given by

$$\hat{\mathbf{s}} = \partial_\alpha \zeta(\alpha, t)/\partial_\alpha s(\alpha, t) = e^{i\theta(\alpha,t)} \quad \text{and} \quad \hat{\mathbf{n}} = i\hat{\mathbf{s}} = ie^{i\theta(\alpha,t)}, \quad (2)$$

with $\theta(\alpha, t)$ the local tangent angle. For the pressure jump term, we use $+$ to denote the side toward which the membrane normal $\hat{\mathbf{n}}$ is directed, and $-$ for the other side. However, for the remainder of this paper, we drop the $+$ and $-$ for ease of notation.

Dividing Eq. (1) by $\Delta\alpha$ and taking the limit $\Delta\alpha \to 0$, we obtain

$$\rho_s hW \partial_{tt}\zeta(\alpha, t) = \partial_\alpha(T(\alpha, t)\hat{\mathbf{s}}) - [p](\alpha, t)W \partial_\alpha s\hat{\mathbf{n}}. \quad (3)$$

The membrane tension $T(\alpha, t)$ is given by linear elasticity [67–69] as

$$T(\alpha, t) = \overline{T} + EhW(\partial_\alpha s(\alpha, t) - 1), \quad (4)$$

where E is the Young's modulus and $\overline{T}$ is the tension in the (initial) undeflected equilibrium state. Equation (3) is made dimensionless by nondimensionalizing length by the membrane's half-chord L, time by L/U, and pressure by $\rho_f U^2$, where ρ_f is the density of the fluid and U is the oncoming flow velocity. The nonlinear, extensible membrane equation becomes

$$R_1 \partial_{tt}\zeta - \partial_\alpha((T_0 + R_3(\partial_\alpha s - 1))\hat{\mathbf{s}}) = -[p]\partial_\alpha s\hat{\mathbf{n}}. \quad (5)$$

The dimensionless membrane mass is $R_1 = \rho_s h/(\rho_f L)$, the dimensionless stretching rigidity is $R_3 = Eh/(\rho_f U^2 L)$ and, finally, $T_0 = \overline{T}/(\rho_f U^2 LW)$ is the dimensionless pretension. The model is linearized for small-amplitude membrane deflections in Sec. III (shown schematically in Fig. 1, right column).

We let $z = x + iy$ to use the complex representation of the xy flow plane. The complex conjugate of the fluid velocity at any point z not on the vortex sheets is a sum of the horizontal background flow with dimensionless speed unity and the flow induced by the bound and free vortex wakes,

$$u_x(z) - iu_y(z) = 1 + \frac{1}{2\pi i}\int_{-1}^1 \frac{\gamma(\alpha, t)}{z - \zeta(\alpha, t)}\partial_\alpha s d\alpha + \frac{1}{2\pi i}\int_0^{s_{\max}} \frac{\gamma(s, t)}{z - \zeta(s, t)}ds, \quad (6)$$

where s is the arc length along the free sheet starting at 0 at the membrane's trailing edge and extending to $s_{\max}$ at the free sheet's far end. To determine the bound vortex sheet strength γ we require that the fluid does not penetrate the membrane, i.e., the kinematic boundary condition. Here γ also represents the jump in the component of the flow velocity tangent to the membrane from the $-$ to the $+$ side, i.e., $\gamma = -[(u_x, u_y) \cdot \hat{\mathbf{s}}]$. The normal components of the fluid and membrane velocities are equal,

$$\text{Re}(\hat{\mathbf{n}}\partial_t\overline{\zeta}(\alpha, t)) = \text{Re}\left(\hat{\mathbf{n}}\left(1 + \frac{1}{2\pi i}\int_{-1}^1 \frac{\gamma(\alpha, t)}{z - \zeta(\alpha, t)}\partial_\alpha s d\alpha + \frac{1}{2\pi i}\int_0^{s_{\max}} \frac{\gamma(s, t)}{z - \zeta(s, t)}ds\right)\right), \quad (7)$$

where $\hat{\mathbf{n}}$ is written as a complex scalar. Solving Eq. (7) for γ on the body requires an additional constraint that the total circulation is zero for a flow started from rest. At each instant, the part of the circulation in the free sheet or, alternatively, the strength of γ where the free sheet meets the trailing edge of the membrane, is set by the Kutta condition which makes the flow velocity finite at the trailing edge. At every other point of the free sheet, γ is set by the criterion that circulation

(the integral of γ) is conserved at material points of the free sheet. The vortex sheet strength $\gamma(\alpha, t)$ is coupled to the pressure jump $[p](\alpha, t)$ across the membrane using a version of the unsteady Bernoulli equation written at a fixed material point on the membrane,

$$\partial_\alpha s \partial_t \gamma + \partial_\alpha(\gamma(\mu - \tau)) + \gamma(\partial_\alpha \tau - \nu\kappa\partial_\alpha s) = \partial_\alpha[p], \tag{8}$$

where μ is the average flow velocity tangent to the membrane, τ and ν are the tangential and normal components of the membrane velocity, respectively, and $\kappa(\alpha, t) = \partial_\alpha\theta/\partial_\alpha s$ is the membrane's curvature. At the trailing edge, $[p]|_{\alpha=1} = 0$. The derivation of Eq. (8) is included in Ref. [[1], Appendix A].

III. SMALL-AMPLITUDE LINEARIZATION

The large-amplitude, nonlinear system described in Sec. II becomes more amenable to analysis in the small-amplitude regime. Here we focus on the computation of eigenmodes and eigenvalues for the three boundary conditions studied in Ref. [1]: fixed-fixed, fixed-free, and free-free membranes. We are thereby able to present the small-amplitude motions of the membranes at larger and smaller membrane densities than in the previous work, and in much greater detail. A similar linearized model was derived in Ref. [37] for the dynamics of a flapping flag. We consider small deflections $y(x, t)$ from the straight configuration, aligned with the flow. Since the membrane stretching factor is $\partial_\alpha s \approx 1 + \partial_x y^2/2$, to linear order $\alpha \approx s \approx x$, all α-derivatives in Eq. (5) are x derivatives, and $\zeta(\alpha, t) \approx \zeta(x, t) = x + iy(x, t)$. At linear order, the tangent and normal vectors are

$$\hat{\mathbf{s}} \approx (1, \partial_x y)^\top, \quad \hat{\mathbf{n}} \approx (-\partial_x y, 1)^\top. \tag{9}$$

The linearized version of the membrane equation is

$$R_1 \partial_{tt} y - T_0 \partial_{xx} y = -[p]. \tag{10}$$

The term in the tension force $T(\alpha, t) = T_0 + R_3(\partial_\alpha s - 1)$ involving R_3 (dimensionless stretching rigidity) is of quadratic order, so the linear dynamics are governed by the dimensionless membrane mass R_1 and the dimensionless pretension T_0. The boundary conditions are

$$\text{fixed-fixed:} \quad y(\pm 1, t) = 0, \tag{11}$$

$$\text{fixed-free:} \quad y(-1, t) = 0, \ \partial_x y(1, t) = 0, \tag{12}$$

$$\text{free-free:} \quad \partial_x y(\pm 1, t) = 0. \tag{13}$$

The dynamics of the membrane are coupled to the fluid flow through the pressure jump term $[p](x, t)$. The linearized version of the pressure jump equation is

$$\partial_t \gamma + \partial_x \gamma = \partial_x[p]. \tag{14}$$

The set of equations is closed by relating the vortex sheet strength $\gamma(x, t)$ back to the membrane position $y(x, t)$, through the kinematic condition, in linearized form:

$$\partial_t y(x, t) = -\partial_x y(x, t) + \frac{1}{2\pi} \int_{-1}^{1} \frac{v(x', t)}{\sqrt{1 - x'^2}(x - x')} \, dx'$$

$$+ \frac{1}{2\pi} \int_{1}^{\ell_w + 1} \frac{\gamma(x', t)}{x - x'} \, dx', \quad -1 < x < 1. \tag{15}$$

Here, we use that $\partial_t \overline{\zeta}(x, t) \approx -i\partial_t y$ and from Eqs. (9), the normal velocity component $\text{Re}(\hat{\mathbf{n}}\partial_t\overline{\zeta}) \approx \partial_t y$. The general solution $\gamma(x, t)$ has inverse square-root singularities at $x = \pm 1$ and so we define $v(x, t)$, the bounded part of $\gamma(x, t)$ by $\gamma = v/\sqrt{1 - x^2}$. The second integral in Eq. (15) represents the velocity induced by the vortex sheet wake, which extends downstream from the membrane on

the interval $1 < x < \ell_w + 1$, $y = 0$. Therefore, the eigenvalue problem assumes a free vortex wake of a given fixed length ℓ_w, which we take to be large (i.e., we assume we start with a deflection that is sufficiently small that we remain in the small-amplitude regime for a long time).

The circulation in the wake,

$$\Gamma(x, t) = -\int_x^{\ell_w+1} \gamma(x', t) \, dx', \tag{16}$$

is conserved along material points of the wake by Kelvin's circulation theorem. At linear order, the wake moves at the constant speed (unity) of the free stream; self-interaction is negligible.

At each time t, the total circulation in the wake, $\Gamma(1, t)$, is set by the Kutta condition, which in linearized form is unchanged, i.e.,

$$v(1, t) = 0. \tag{17}$$

Using the system of Eqs. (10), (14), (15), and (17), we solve for the following unknowns: the motion of the membrane and the strengths of the vortex sheets along the membrane and in the wake.

For the linearized system, we may write solutions in the following form:

$$y(x, t) = Y(x)e^{i\sigma t}, \tag{18}$$

$$\gamma(x, t) = g(x)e^{i\sigma t}, \tag{19}$$

$$v(x, t) = V(x)e^{i\sigma t}, \tag{20}$$

$$\Gamma(1, t) = \Gamma_0 e^{i\sigma t}, \tag{21}$$

where Y, g, V, and Γ_0 are components of eigenmodes with complex eigenvalues $\sigma = \sigma_R + i\sigma_I \in \mathbb{C}$. The real parts of the eigenvalues are the angular frequencies and the imaginary parts are the temporal growth rates. If $\sigma_I > 0$, small perturbations decay exponentially and the mode is stable, while if $\sigma_I < 0$, small perturbations grow exponentially and the mode is unstable. If $\sigma_I = 0$, the mode is neutrally stable.

We wish to identify the region of R_1–T_0 space in which unstable eigenmodes exist and, when there are multiple unstable modes, identify the fastest growing mode.

Since Γ is conserved at material points of the free vortex sheet as they move downstream (at speed 1) and the material point at location $x \geqslant 1$ at time t was at location $x = 1$ at time $t - (x - 1)$, we can write

$$\Gamma(x, t) = \Gamma_0 e^{i\sigma(t-(x-1))} = \Gamma_0 e^{-i\sigma(x-1)} e^{i\sigma t}, \quad 1 < x < \ell_w + 1, \tag{22}$$

$$\gamma(x, t) = \partial_x \Gamma(x, t) = -i\sigma \Gamma_0 e^{-i\sigma(x-1)} e^{i\sigma t}, \quad 1 < x < \ell_w + 1, \tag{23}$$

using Eq. (21). Inserting the eigenmodes Eqs. (18)–(21) into the governing equations, Eqs. (10) and (15), yields

$$-\sigma^2 R_1 Y = T_0 \partial_{xx} Y - i\sigma \int_{-1}^1 g \, dx - g \tag{24}$$

and

$$i\sigma Y = -\partial_x Y + \frac{1}{2\pi} \int_{-1}^1 \frac{V(x')}{\sqrt{1-x'^2}(x-x')} \, dx' - \frac{1}{2\pi} i\sigma \Gamma_0 \int_1^{\ell_w+1} \frac{e^{-i\sigma(x'-1)}}{x-x'} \, dx', \quad -1 < x < 1, \tag{25}$$

respectively. Because σ appears in the exponential in the second integral in Eq. (25), this is a nonlinear eigenvalue problem.

A. Numerical method for finding the eigenvalues and eigenmodes

We solve the nonlinear eigenvalue problem iteratively. At each iteration, we have an approximation σ_0 to a given eigenvalue σ. We approximate the equations as a quadratic eigenvalue problem

$$[\sigma^2 A_2 + \sigma A_1 + A_0(\sigma_0)]w = 0, \tag{26}$$

where the matrices A_2, A_1, A_0 are known from Eqs. (24) and (25), and $g(x) = V(x)/\sqrt{1-x^2}$. The eigenvector w consists of (a) values of the eigenmodes, defined as $Y(x)$ on the Chebyshev grid $\{x_j = \cos\theta_j, \ \theta_j = (j-1)\pi/m, \ j = 1, \ldots, m+1\}$ and (b) the scalar Γ_0. The term $A_0(\sigma)w$ includes the exponential integral involving σ in Eq. (25) as well as terms that are constant in σ. In the exponential integral, σ is fixed at σ_0, the value of σ from the previous iteration, resulting in the quadratic eigenvalue problem Eq. (26), which is solved using `polyeig` in MATLAB. Equation (26) has $2m + 4$ eigenvalue solutions. As in Ref. [37], we define an error function as the difference between σ_0 and the eigenvalue (out of the $2m + 4$ possibilities) closest to it. We also compute the derivatives of the error function (i.e., the Jacobian matrix) with respect to σ_R and σ_I using finite differences at the initial iterate, and update it at subsequent iterates using Broyden's approximate formula [70]. The error function and Jacobian define the search direction (via Newton's formula) for the next iterate. With this approach, we obtain superlinear convergence to a given eigenvalue. By using a wide range of initial guesses, we obtain convergence to various eigenvalues and corresponding eigenmodes.

The numerical solution procedure followed in the current work differs from Ref. [37]. There we used a continuation method, which for the current problem would start from the analytical solution for each eigenvalue in the limit $R_1, T_0 \gg 1$, and use the solution at a given (R_1, T_0) as an initial guess for slightly smaller (R_1, T_0) [continuing to smaller and smaller (R_1, T_0)]. We find that this method fails to find solutions at certain (R_1, T_0) and therefore at smaller values also, so we use a more robust approach here. We compute a large set of eigenvalues at each (R_1, T_0) using a large grid of initial eigenvalue guesses in the complex plane covering in most cases $\sigma_R \in [-8, 8]$ and $\sigma_I \in [-3, -0.5]$. For each initial guess, we perform the eigenvalue iteration described above until it converges. This reveals the basins of attraction of the eigenvalues under Broyden's iteration, which shows that the imaginary part is not as important as the real part of the eigenvalue guess (especially for large R_1 values). We note that in the system of Eqs. (24) and (25) the eigenvalue σ appears in powers of $i\sigma$. For each solution $\{i\sigma, w\}$, the complex conjugate $\{-i\bar{\sigma}, \bar{w}\}$ is also a solution, so we need only compute one member of the pair, and obtain the other by conjugation. For the eigenvalue $i\sigma = i\sigma_R - \sigma_I$, the conjugate is $-i\bar{\sigma} = -i\sigma_R - \sigma_I$; i.e., the sign of σ_R is reversed. Thus we can restrict to $\sigma_R \geqslant 0$.

We now present typical examples of our eigenmode computations. Throughout the paper, we use $m = 120$ for the Chebyshev grid, unless noted otherwise. Comparisons between $m = 80$ and 120 (as well as 240) are presented in Appendix A. Figure 2 shows results for $(R_1, T_0) = (10^{-1}, 10^{-0.27})$ with both membrane edges fixed. The coloring in Figs. 2(a) and 2(b) indicates the converged values of σ_R [Fig. 2(a)] and σ_I [Fig. 2(b)] over a grid of initial eigenvalue guesses in the complex plane spanning 320 values in the real direction and four values in the imaginary direction. In Fig. 2(c), we plot the 25 distinct eigenvalues found with this set of initial guesses and in Fig. 2(d), the corresponding eigenmodes from the most unstable (smallest — or most negative —σ_I) on the left to the most stable (largest σ_I) on the right. The vertical black line in Fig. 2(d) separates the (only) unstable mode (on its left) from the stable modes (on its right). The unstable mode loses stability through divergence as is evident from Fig. 2(c), where the associated eigenvalue has $\sigma_R \approx 10^{-9}$ and $\sigma_I < 0$. We also illustrate with a red circle in Figs. 2(a) and 2(b) an instance of an initial guess that gives rise to this mode. The converged σ values are more sensitive to the real than to the imaginary part of the initial guess, which motivates the wider range of σ_R used here and subsequently.

In Fig. 3, we show another example of the eigenvalue computation for fixed-fixed membranes, with larger membrane mass and pretension: $(R_1, T_0) = (10^3, 10^{1.5})$. In Figs. 3(a) and 3(b), we use
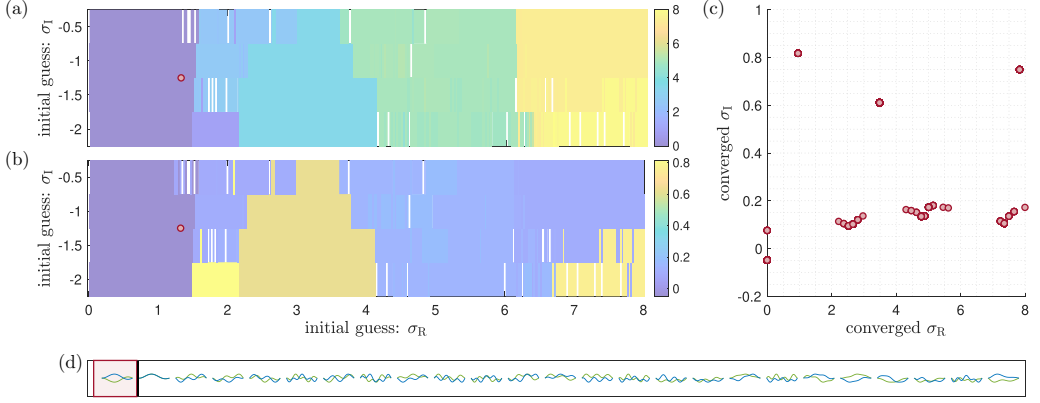
FIG. 2. Fixed-fixed eigenvalues and eigenmodes with $R_1 = 10^{-1}$ and $T_0 = 10^{-0.27}$. Computed σ_R [(a), values in color bars at right] and computed σ_I [(b), values in color bars at right], both plotted over the initial guess complex plane (c). The distinct eigenvalues generated by the numerical method replotted as red dots in the (σ_R, σ_I) plane. (d) The corresponding eigenmodes [Re($Y(x)$) in green, Im($Y(x)$) in blue] from the only unstable one (with negative σ_I) on the left to the most stable one (largest σ_I) on the right. The vertical black line separates the unstable mode (on its left) and stable modes (on its right).

a grid of initial eigenvalue guesses spanning 640 values in the real direction and six values in the imaginary direction. For smaller R_1 (as in Fig. 2), the converged σ vary more with the initial choice of σ_I compared to the larger R_1 here, where the converged eigenvalues are independent of the initial σ_I, and depend only on the initial σ_R.

Since a generic perturbation is a superposition of all the eigenmodes multiplied by $e^{i\sigma t} = e^{i\sigma_R t}e^{-\sigma_I t}$, we classify the stability of generic perturbations in the (R_1, T_0) parameter space based on the value of $\sigma_R + i\sigma_I$ for the smallest σ_I at a given (R_1, T_0):

(1) $\sigma_I > 0$: stable
(2) $\sigma_I = 0$: stability boundary location
(3) $\sigma_I < 0$ and $\sigma_R = 0$: divergence (static instability)
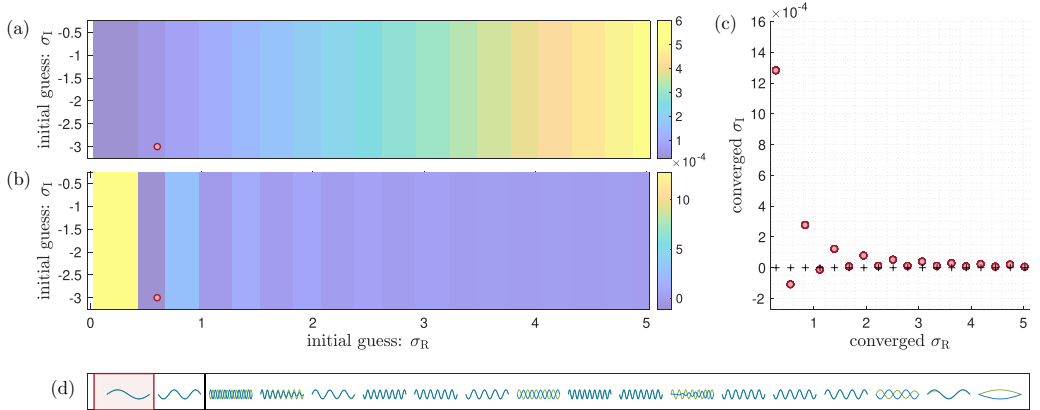(4) $\sigma_I < 0$ and $\sigma_R \neq 0$: flutter and divergence

FIG. 3. Fixed-fixed eigenvalues and eigenmodes with $R_1 = 10^3$ and $T_0 = 10^{1.5}$ and other quantities as described in Fig. 2.
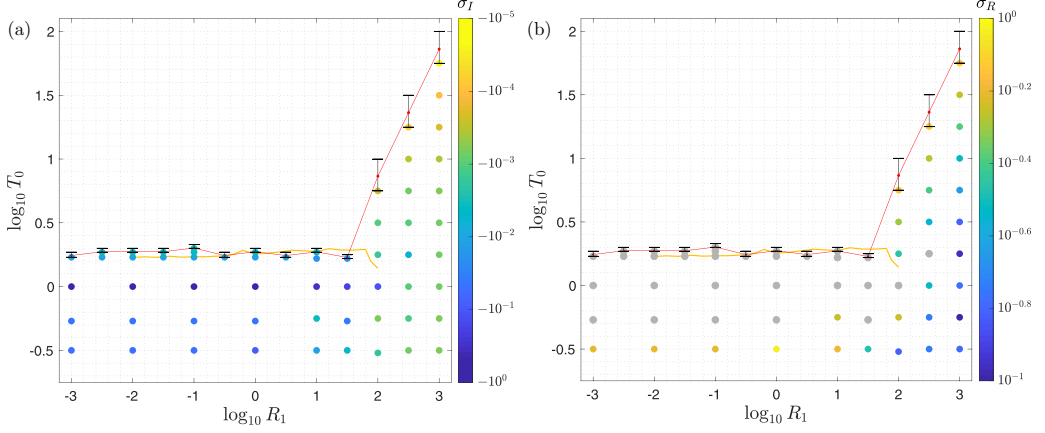
FIG. 4. The region in R_1–T_0 space in which the fixed-fixed membrane is unstable. The red line and red dots indicate the position of the stability boundary computed by linear interpolation between σ_I of the smallest T_0 that gives a stable membrane and the σ_I of the largest T_0 that gives an unstable membrane (shown in the error bars). The colors of the dots below the stability boundary label: (a) The imaginary parts of the eigenvalues (σ_I) corresponding to the most unstable modes. They represent the temporal growth rate. (b) The real parts of the eigenvalues (σ_R) for the most unstable modes, representing the angular frequencies. The gray dots correspond to modes that lose stability by divergence and have $\sigma_R \leqslant 10^{-9}$. The orange line that spans $\log_{10} R_1 \in [-2, 2]$ represents the stability boundary computed numerically in Ref. [1].

IV. FIXED-FIXED MEMBRANES

We start with membranes that have both edges fixed at zero deflection [satisfying Eq. (11)]. We plot the stability boundary as the red dots connected by red lines in Figs. 4(a) and 4(b). Below and to the right is the unstable region. The red dots are computed by linear interpolation of σ_I between neighboring T_0 values (shown by the horizontal black bars) that bracket the boundary: All σ_I are positive at the larger of the T_0 values and above, but one σ_I is negative at the smaller of the T_0 values.

The stability boundary (red line) agrees well with that of our nonlinear time-stepping simulations (orange line, from Ref. [1]) and with the results of Ref. [3]. For each R_1, an eigenmode first becomes unstable when the pretension T_0 drops below a critical value $T_{0C}(R_1)$. For $R_1 < 10^2$, $T_{0C}(R_1) \in [1.7, 2]$, almost independent of R_1. In our nonlinear, unsteady simulations [1], we found a similar range of $T_{0C}(R_1)$, [1.7,1.92], for $R_1 < 10^{1.5}$. The small discrepancy could arise from the δ smoothing on the free vortex sheet (that is not used in the eigenvalue solution but is used in the time-stepping simulation). Another possible explanation (as stated in Ref. [37]) is that in the time-stepping simulation [1], the wake grows from zero length but in the current eigenvalue problem the wake has fixed length ℓ_w. In our simulations, we use $\ell_w = 39$, and the modes are essentially unchanged at larger ℓ_w. In Ref. [1], we were not able to compute the upward sloping portion of the stability boundary for $R_1 > 10^{1.5}$ using the unsteady simulations, due to the slow growth/decay of small perturbations with large R_1.

In Fig. 4, the colored dots give the imaginary [Fig. 4(a)] and real parts [Fig. 4(b)] of the most unstable eigenvalues (with corresponding eigenmodes shown later in Fig. 5). The gray dots in Fig. 4(b) indicate negative σ_I and nearly zero σ_R ($\sigma_R \leqslant 10^{-9}$) for the most unstable eigenmode, which corresponds to divergence. The colored dots in Fig. 4(b) indicate a nonzero real part (value in color bar at right) for the most unstable eigenmode, corresponding to flutter and divergence. Within the instability region (region below the red line), we find that for a fixed T_0, the fastest growing mode has a growth rate (σ_I) that generally decreases in magnitude as R_1 increases. We also find that membranes with $R_1 \lesssim 10^{1.5}$, in general, lose stability by divergence for $T_0 \in (10^{-0.5}, T_{0C}(R_1)]$
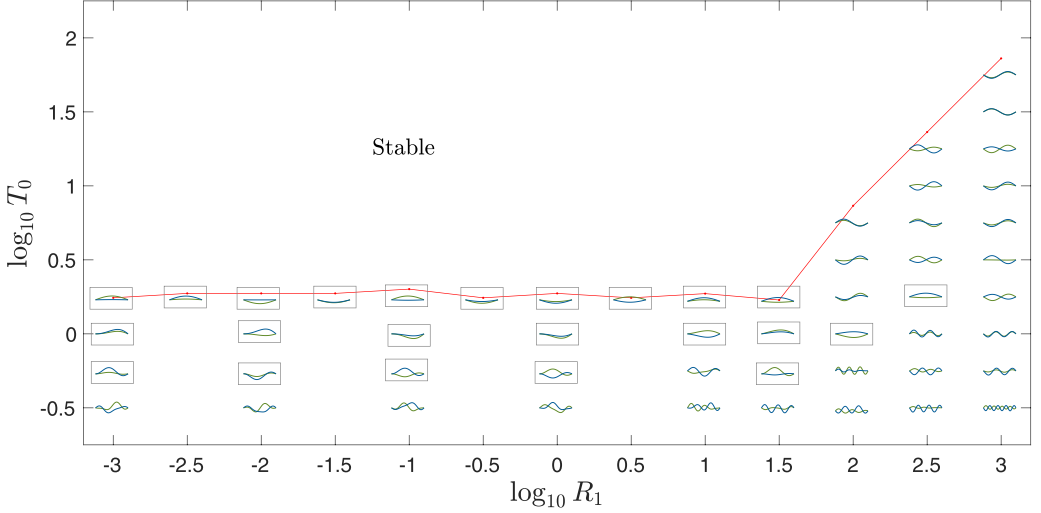
FIG. 5. The shapes $Y(x)$ of the most unstable eigenmodes as a function of R_1 and T_0 in the fixed-fixed case. The real and imaginary parts of $Y(x)$ are shown in green and blue, respectively. Each shape is scaled both vertically and horizontally to fit within the plot. The shapes are superposed on the same stability boundary (red line) as in Fig. 4. Modes exhibiting a divergence instability have a gray rectangle outline.

but then for a smaller T_0 ($\lesssim 10^{-0.5}$), by flutter and divergence. Heavier membranes generally lose stability by flutter and divergence for $T_0 \in (10^{0.25}, T_{0C}(R_1)]$.

In the limit $R_1, T_0 \gg 1$, the fluid pressure is negligible and the linearized membrane Eq. (10) reduces to the homogeneous wave equation,

$$R_1 \partial_{tt} y - T_0 \partial_{xx} y = 0, \tag{27}$$

which after substituting Eq. (18) becomes

$$-\sigma^2 R_1 Y - T_0 \partial_{xx} Y = 0. \tag{28}$$

The eigenmodes are linear combinations of $\cos(kx)$ and $\sin(kx)$, with $k = \pm\sigma\sqrt{R_1/T_0}$, satisfying the boundary conditions Eq. (11). Nontrivial linear combinations exist for k values for which the determinant of the matrix

$$\begin{pmatrix} \sin(-k) & \cos(-k) \\ \sin(k) & \cos(k) \end{pmatrix} \tag{29}$$

vanishes, which occurs at $k = n\pi/2$ for $n \in \mathbb{Z}_{>0}$. Each k gives a pair of eigenvalues,

$$\sigma = \pm k\sqrt{\frac{T_0}{R_1}}, \tag{30}$$

and eigenmodes of the form

$$Y(x) = \sin\left(\frac{n\pi}{2}(x+1)\right), \tag{31}$$

for $n \in \mathbb{Z}_{>0}$ and $-1 \leqslant x \leqslant 1$, where the amplitude is arbitrary.

Similar to Ref. [37], in the limit of $R_1, T_0 \gg 1$, Eq. (30) shows that the frequency scales as $\sqrt{T_0/R_1}$. We have observed this in our simulations: σ_R is approximately constant along lines of constant T_0/R_1 in the upper right portion of Fig. 4(b) (toward the vacuum limit). At smaller R_1, the angular frequency is less sensitive to the membrane pretension.

The numerical results for the eigenvalues (red dots) shown in Fig. 3(c) show excellent agreement with the analytical form (30) of σ (black pluses), with very small imaginary parts (vertical axis). In Fig. 3(d), there are two unstable modes [$n = 2$ and 4 in Eq. (31)], which are also the unstable modes that were found in Ref. [3] for large values of R_1 and T_0.

In Fig. 5, we plot again the instability region in the R_1–T_0 parameter space for fixed-fixed membranes, but with the eigenmode shapes corresponding to the most unstable eigenvalues in Fig. 4. The real and imaginary parts of the eigenmode $Y(x)$ are shown in green and blue, respectively. We place gray rectangles around the modes that lose stability by divergence. For $R_1 < 10^2$ and T_0 just below T_{0C}, the unstable eigenmode is a single-hump shape that is nearly fore-aft symmetric. As the pretension is decreased further below T_{0C}, the divergent eigenmode becomes asymmetric, its maximum deflection point shifting toward the trailing edge. This agrees with Ref. [[3], Fig. 10]. In the divergence region of Fig. 5 when $T_0 = 10^0$ and R_1 decreases from 10^2 to 10^{-1}, the maximum deflection point also shifts from the midchord toward the trailing edge, in agreement with Ref. [[3], Fig. 5]. For heavier membranes ($R_1 \geqslant 10^2$), the membrane loses stability with an even-numbered mode shape through flutter and divergence. In particular, the second mode ($n = 2$) is the most unstable mode for $R_1 \geqslant 10^2$ and $T_0 \in [10^{0.5}, T_{0C}(R_1)]$, as well as $(R_1, T_0) = (10^2, 10^{0.25})$ and $(10^3, 10^{0.25})$. Decreasing the pretension value below $10^{0.25}$, the fourth mode ($n = 4$) becomes the most unstable for $R_1 > 10^2$, followed by the sixth mode at $(R_1, T_0) = (10^2, 10^{-0.25})$, $(10^{2.5}, 10^{-0.5})$. For heavy membranes with decreasing T_0, the most unstable mode apparently moves to progressively higher even-numbered modes.

We now study in more detail how the eigenvalues change in R_1–T_0 space by examining what happens when T_0 passes through the stability boundary. We track the stable and unstable modes using a grid of initial eigenvalue guesses in the complex plane covering $\sigma_R \in (0, 8]$ and $\sigma_I \in [-3, 3]$, with 160 values in the real direction and 13 values in the imaginary direction. As can be observed in Fig. 5, in general, as we move to smaller T_0 values, higher wave-number modes become the most unstable ones. We now consider the instability of higher wave-number modes as we cross the stability boundary by fixing two values of R_1 and decreasing T_0, while tracking the real and imaginary parts of the computed eigenvalues.

In Fig. 6, we show the real (bottom row) and imaginary parts (top row) of the eigenvalues for $R_1 = 10^3$ (left column) and 10^1 (right column) while decreasing T_0. The colors show the normalized root mean square (RMS) slope of each membrane eigenmode on the Chebyshev mesh, defined by

$$Y'_{\mathrm{RMS}} := \sqrt{\int_{-1}^{1} \left| \frac{dY}{dx} \right|^2 dx \bigg/ \int_{-1}^{1} |Y|^2 dx}, \tag{32}$$

which is a measure of the waviness of each mode. Each branch that possesses approximately the same color (lying in a particular, small range of Y'_{RMS}) indicates a distinct mode. At the highest mass ($R_1 = 1000$), Figs. 6(a) and 6(b), we connect the eigenvalues by polygonal lines for the modes that are sufficiently distinct from the others—the seven lowest wavenumber modes. The branches in Fig. 6(a) are somewhat jagged when $|\sigma_I|$ drops below 10^{-5}. The corresponding σ_R [Fig. 6(b)] vary much more smoothly, probably because their magnitudes are larger relative to numerical errors. The blue branch with the most negative σ_I values first becomes unstable (σ_I changes from positive to negative) at $T_0 \approx 10^{1.87}$, which coincides with the loss of stability in Fig. 5. The mode associated with this blue branch is the second mode [$n = 2$ in Eq. (31)]. The next branch to become unstable corresponds to the fourth mode ($n = 4$) at $T_0 \approx 10^{1.56}$ and then the sixth mode ($n = 6$) at $T_0 \approx 10^{1.41}$. Representative mode shapes at the smallest $T_0 = 10^{1.2}$ are shown to the left of Fig. 6(a), for the three unstable branches ($n = 2, 4,$ and 6) and four stable branches ($n = 1, 3, 5,$ and 7). The Y'_{RMS} values that correspond to these seven lowest wave-number modes are approximately those of the analytical eigenmodes in (31), $n\pi/2$ for $n = 1, 2, \ldots, 7$. We also illustrate examples at larger T_0 values for the $n = 2$ and 4 branches and find that the mode shapes are almost unchanged. In particular, we note that the seven modes shown to the left of $T_0 = 10^{1.2}$ all remain approximately the same across the corresponding colored branch for $T_0 \in [10^{1.2}, 10^{1.875}]$. In Fig. 6, we focus on the
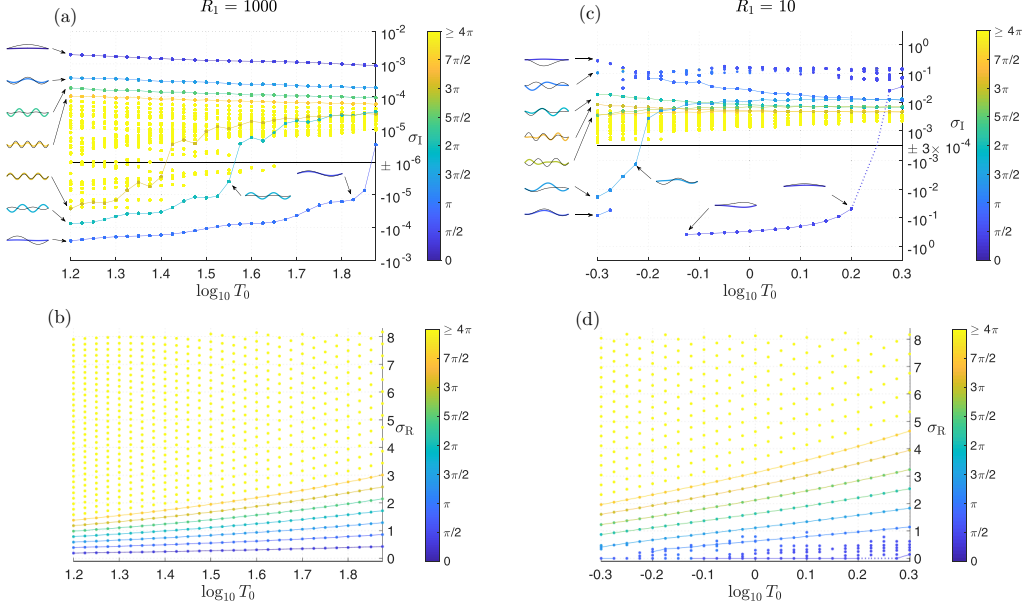
FIG. 6. For two values of membrane mass (R_1), 10^3 (left column) and 10^1 (right column), the imaginary [(a), (c)] and real parts [(b), (d)] of the eigenvalues versus pretension (T_0) for fixed-fixed membranes. The coloring represents the RMS of the membrane's slope, Y'_{RMS} (32) for each (R_1, T_0) pair. The horizontal black lines in the top panels located at (a) $\sigma_I = \pm 10^{-6}$ and (c) $\sigma_I = \pm 3 \times 10^{-4}$ distinguish stable modes (above) and unstable modes (below). To the left of and within (a) and (c), we show typical modes for branches with $Y'_{RMS} < 4\pi$.

lowest wave-number shapes, as the higher wave-number shapes (yellow dots) are not numerically resolved. The odd-numbered modes remain stable for all values of T_0 shown. As we decrease the pretension T_0, the number of distinct modes found—with the range of initial guesses that we are using—increases. This is indicated by the higher density of dots at smaller T_0 in Fig. 6(b). Figures 6(c) and 6(d) show the corresponding data for a smaller membrane mass, $R_1 = 10$. The modes deviate more from the analytical expression of Eq. (31) and change more significantly across T_0, compared to Fig. 6(a). Representative modes at the smallest $T_0 = 10^{-0.3}$ are shown at the left side of Fig. 6(c). The shape of the curves that connect the real part of the eigenvalues associated with a particular mode shape (lower panels) seems to be similar for the two mass densities. However, for the smaller mass ($R_1 = 10$) there is a disordered band of dark blue dots (with $Y'_{RMS} < \pi/4$) that are stable [$\sigma_I \approx 10^{-1}$ is Fig. 6(c)] and have low frequency [$\sigma_R \lesssim 1$ in Fig. 6(d)].

To summarize, in agreement with Ref. [3], we have found that the stability boundary has an upward slope for $R_1 \geqslant 10^2$, whereas for $R_1 < 10^2$ the critical T_0 for instability lies in [1.7,2], almost independent of R_1. When R_1 and T_0 are dominant over fluid pressure forces, the membrane eigenmodes tend to neutrally stable sinusoidal functions. When the fluid forces are small but nonnegligible, the mode shapes are similar, with the even-numbered modes becoming unstable with very small growth rates, starting with the second modes. We find roughly two regions: (a) at small R_1, divergence occurs with the most unstable mode becoming more fore-aft asymmetric as we decrease T_0 and (b) at large R_1, flutter and divergence occur with approximately sinusoidal eigenmodes. In both of these regions, the most unstable modes become more wavy at smaller T_0. We have extended previous studies of the fixed-fixed membrane to a wider range of R_1–T_0 space. Next, we study cases in which the membrane ends can move freely, which are less well-known.
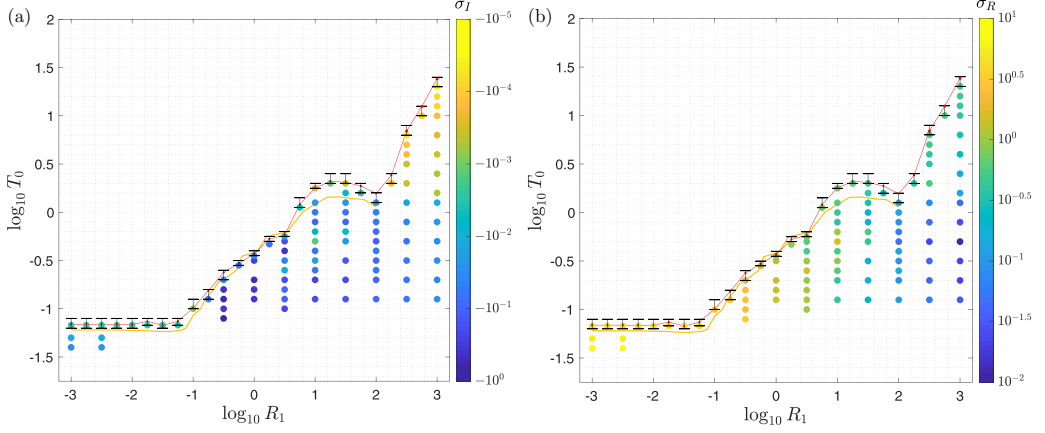
FIG. 7. The region in R_1–T_0 space in which the fixed-free membrane is unstable. The red line and red dots indicate the position of the stability boundary computed using linear interpolation between σ_I of the smallest T_0 that gives only stable eigenmodes and the σ_I of the largest T_0 that gives an unstable eigenmode (shown in the error bars). The color of the dots below the stability boundary labels: (a) The imaginary part of the eigenvalue (σ_I) corresponding to the most unstable modes. It represents the temporal growth rate. (b) The real part of the eigenvalues (σ_R) for the most unstable mode, representing the angular frequency. The orange line that spans $R_1 \in [10^{-3}, 10^2]$ represents the stability boundary computed numerically in Ref. [1].

V. FIXED-FREE MEMBRANES

We now investigate the stability of membranes with the leading edge fixed and the trailing edge free to move vertically, i.e., satisfying the boundary conditions Eq. (12). In Ref. [1], we found that with one end free, the membrane has a wider range of unsteady dynamics. In particular, in the steady-state large-amplitude regime, we showed in Ref. [1] that this set of boundary conditions has a mixture of periodic and chaotic dynamics as opposed to the steady single-hump solutions observed in fixed-fixed membranes. In the small-amplitude (growth) regime, we will now show that the eigenmodes can also be somewhat more complicated.

In Fig. 7, we plot the imaginary [Fig. 7(a)] and real parts [Fig. 7(b)] of the most unstable eigenvalues in the region of instability for the fixed-free membranes in R_1–T_0 space. The red line marks the boundary where the eigenvalues change from all $\sigma_I > 0$ (stable membranes) to at least one $\sigma_I < 0$ (unstable membranes), analogous to Fig. 4. As in the fixed-fixed case, the stability boundary moves to larger pretension (T_0) values with increasing membrane mass (R_1), but starting at much smaller R_1 now ($\geqslant 10^{-1}$). As R_1 decreases below 10^{-1}, the critical pretension reaches a lower plateau.

The stability boundary of the current study is compared against the boundary from the nonlinear study in Ref. [1] (orange line). Their shapes are very similar and there is good agreement especially for $R_1 \in [10^{-0.75}, 10^{0.5}]$. As in Fig. 4, the discrepancy may be due to δ smoothing used on the free vortex sheet of Ref. [1], the choice of the vortex wake ℓ_w, or the number of Chebyshev nodes ($m + 1$) on the membrane. In the unsteady simulations (orange line), we used $m = 40$ because the simulations require more computing time, but in the current paper (red line) we used $m = 120$. The eigenvalue solver shows that the boundary slopes upward over $R_1 \in [10^2, 10^3]$, where it was difficult to obtain accurate results with the unsteady simulations.

The trends of the most unstable eigenvalues (colored dots) are similar to the fixed-fixed case (Fig. 4) in some ways: the growth rates σ_I generally become larger in magnitude at smaller T_0 and smaller R_1 [Fig. 7(a)] and the growth rates vary nonmonotonically with T_0 at intermediate R_1 ($[10^{0.5}, 10^{1.5}]$ for fixed-free and smaller R_1 for fixed-fixed). A difference is the slight decrease in growth rates as R_1 decreases below 10^{-1} for the fixed-free case, which does not occur in the
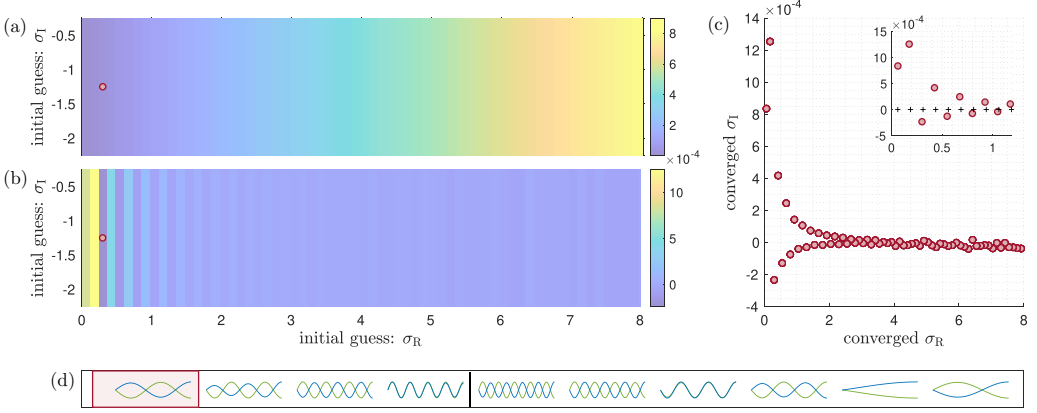
FIG. 8. Fixed-free eigenvalues and eigenmodes with $R_1 = 10^3$ and $T_0 = 10^{0.8}$. Computed σ_R [panel (a), values in color bars at right] and computed σ_I [(b), values in color bars at right], both in the initial guess complex plane. (c) The computed eigenvalues replotted as red dots in the (σ_R, σ_I) plane. The inset in (c) shows the ten computed eigenvalues (red ○) that correspond to the eigenmodes shown in (d). The analytical form of the eigenvalues is $\sigma = ((n - 1/2)\pi/2)\sqrt{T_0/R_1} = ((n - 1/2)\pi/2)\sqrt{10^{0.8}/10^3}$ for $n = 1, \ldots, 10$ (black pluses).

fixed-fixed case. For $R_1 \in [10^2, 10^3]$, the fixed-free growth rates are qualitatively similar to those in the fixed-fixed case above $T_0 = 10^{0.1}$. Below this value, however, the fixed-free growth rates jump by more than an order of magnitude. In both cases, the real parts of the eigenvalues [the angular frequencies σ_R, Fig. 7(b)] generally decrease with decreasing T_0 and with increasing R_1, particularly at the largest R_1. Below $R_1 = 10^{1.5}$, the frequencies are very different: divergence ($\sigma_R \approx 0$) does not occur in the fixed-free case but is common in the fixed-fixed case.

To consider the eigenmodes in the fixed-free case, we again start with R_1 and $T_0 \gg 1$, so the fluid forcing is negligible and the eigenmodes are again solutions of Eq. (27), i.e., nontrivial linear combinations of $\cos(kx)$ and $\sin(kx)$, with $k = \pm\sigma\sqrt{R_1/T_0}$, but satisfying the boundary conditions Eq. (12) now. The k are now those for which the determinant of

$$\begin{pmatrix} \sin(-k) & \cos(-k) \\ \cos(k) & -\sin(k) \end{pmatrix} \tag{33}$$

is zero, which leads to $k = (n - 1/2)\pi/2$ for $n \in \mathbb{Z}_{>0}$, corresponding eigenvalues $\sigma = \pm k\sqrt{T_0/R_1}$, and eigenmodes now of the form

$$Y(x) = \sin\left(\left(n - \frac{1}{2}\right)\frac{\pi}{2}(x + 1)\right), \tag{34}$$

for $n \in \mathbb{Z}_{>0}$ and $-1 \leqslant x \leqslant 1$. Each mode has one quarter wavelength less than that of the corresponding fixed-fixed mode, so the trailing edge has zero slope.

Figure 8 shows an example of how the computed eigenvalues [real parts in Fig. 8(a) and imaginary parts in Fig. 8(b)] vary over a grid of initial guesses in the complex plane for a fixed-free membrane with $(R_1, T_0) = (10^3, 10^{0.8})$ in the large R_1 region near the stability boundary. The quantities plotted are analogous to those in Fig. 3. The grid of initial eigenvalue guesses in the complex plane covers $\sigma_R \in (0, 8]$ and $\sigma_I \in [-2, -0.5]$, spanning 640 values in the real direction and four values in the imaginary direction. As in Fig. 3, we see that for large R_1 (10^3) and moderately large T_0 $(10^{0.8})$, the eigenvalues obtained by the numerical method depend mainly on the real part of the initial eigenvalue guess. However, here we see that there is more variation in the computed eigenvalues with respect to the choice of initial σ_R compared to Fig. 3, where the vertical bands of constant real [Fig. 3(a)] and imaginary parts [Fig. 3(b)] of σ are wider. This may be due to the
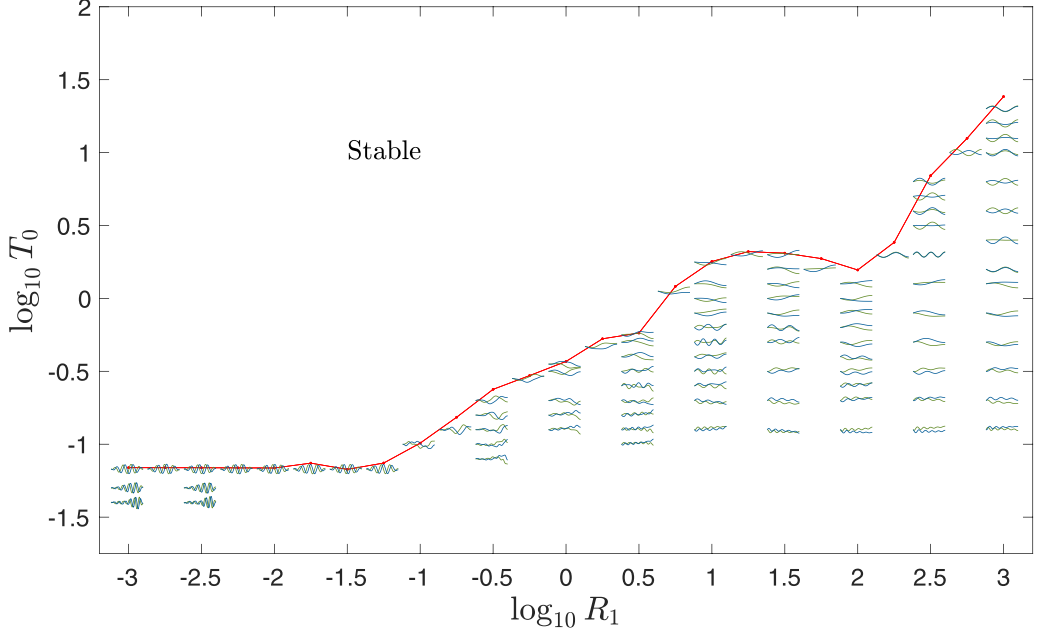
FIG. 9. The shapes $Y(x)$ of the most unstable eigenmode as a function of R_1 and T_0 in the fixed-free case. The real part of $Y(x)$ is shown in green and the imaginary part of $Y(x)$ is shown in blue. Each shape is scaled, both vertically and horizontally, to fit within the plot. The shapes are superposed on the same stability boundary (red line) as in Fig. 7.

smaller value of T_0 considered in Fig. 8 ($10^{0.8}$ as opposed to $10^{1.5}$ in Fig. 3). As we decrease the membrane pretension (T_0), the number of distinct modes found (with our range of initial guesses) typically increases [e.g., Figs. 6(a) and 6(b)]. The numerically computed eigenvalues from Figs. 8(a) and 8(b) are replotted as red dots in the (σ_R, σ_I) plane in Fig. 8(c), and those at the smallest σ_R, shown in the inset, agree closely with the analytical form Eq. (30) with $k = (n - 1/2)\pi/2$ for $n \in \mathbb{Z}_{>0}$ (black pluses in inset; note there is close agreement in the imaginary part due to the small axis scale). Many eigenmodes are found with wavelengths decreasing down to the mesh scale, but in Fig. 8(d) we show the ten modes with largest wavelengths [i.e., $n = 1, \ldots, 10$ in Eq. (34)], those that are best resolved numerically. Starting from the left, the most unstable modes have $n = 3, 5,$ 7, and 9, while $n = 10, 8, 6, 4, 1,$ and 2 are stable. Except for $n = 1$, the modes with even and odd n have the opposite stability behavior. Here we omit the computed modes with the highest wave numbers because they (and the corresponding eigenvalues) are not numerically converged. For the large-R_1, large-T_0 limit solved analytically in Eq. (34), we have a quadratic eigenvalue problem. When discretized by the numerical method in Sec. III A, we have $2m + 2$ eigenmodes $Y(x)$ varying from low wave-number modes to very high wave-number modes that oscillate on the mesh scale (due to the discretized second x derivative). For more general R_1 and T_0, we have a nonlinear eigenvalue problem, but still have eigenmodes that oscillate on the mesh scale, and are thus not resolved (i.e., not close to a continuum solution). Therefore, we focus on the lower wave-number eigenmodes—those with Y'_{RMS} [defined in Eq. (32)] below a threshold near 4π, or about four wavelengths for a sinusoidal $Y(x)$—which we can resolve well with $m = 120$ grid points.

In Fig. 9, we examine the variations in the most unstable eigenmodes in the same (R_1, T_0) space as Fig. 7, corresponding to the eigenvalues shown there. There is a narrow band with $R_1 = 10^0$ and $10^{-0.65} < T_0 < 10^{-0.55}$ where our initial guesses all produced $\sigma_I > 0$ and so the modes are stable, and therefore none are shown in this range. Similar small bands of stability between unstable regions were also observed in Refs. [33,35] for fixed-fixed membranes. The shapes do not change noticeably
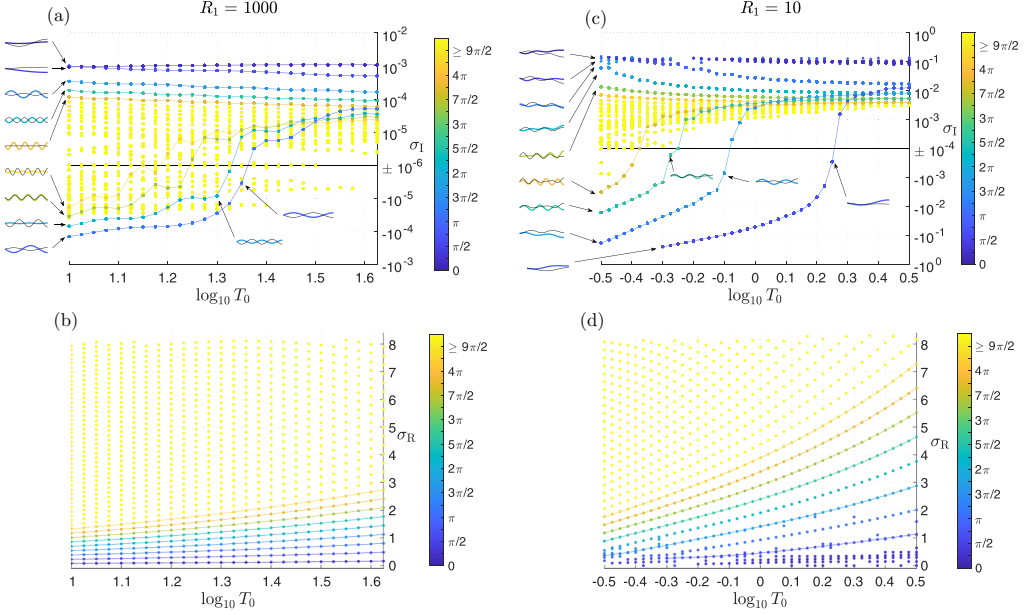
FIG. 10. For two values of membrane mass (R_1), 10^3 (left column) and 10^1 (right column), the imaginary [(a), (c)] and real parts [(b), (d)] of the eigenvalues versus pretension (T_0) for fixed-free membranes. The coloring represents the RMS of the membrane's slope, $Y'_{\rm RMS}$, for each (R_1, T_0) pair given by Eq. (32). The horizontal black line in the top panels located at (a) $\sigma_{\rm I} = \pm 10^{-6}$, (c) $\sigma_{\rm I} = \pm 10^{-4}$ distinguishes stable modes (above) and unstable modes (below). We also show typical modes that correspond to each branch with $Y'_{\rm RMS} < 9\pi/2$.

for the more irregular motions at $R_1 \in [10^{-3}, 10^{-1.25}]$ (the eigenvalues in Fig. 7 were also nearly constant in this region). At these smallest R_1 values, the deflection at the free end is nearly zero. As we decrease T_0 for $R_1 \leqslant 10^{-2.5}$, the ripples move toward the trailing edge of the membrane while maintaining nearly zero deflection at that end. Close to the stability boundary, all the shapes for $R_1 \in [10^{0.75}, 10^2]$ are also nearly alike. At moderate values of R_1 ($[10^{-1}, 10^2]$) the maximum deflection occurs in most cases at the trailing edge of the membrane. At these and larger values of R_1, the mean slope of the membrane is nonzero. In a similar region of R_1 (i.e., $[10^{-1}, 10^{1.75}]$) fixed-fixed membranes become unstable with a single hump, losing stability via divergence. Fixed-free membranes, however, become unstable by flutter and divergence. When T_0 is below $10^{-0.2}$, the most unstable mode changes to a wavier profile—the mode wave number increases with decreasing T_0. Similar to the fixed-fixed case where even-numbered modes become unstable for large R_1, we see in Fig. 9 that heavy fixed-free membranes ($R_1 > 10^2$) with $T_0 \in [10^{0.2}, T_{0C}(R_1)]$ become unstable with an odd-numbered mode—the third mode (the first mode is stable). At $T_0 < 10^{0.2}$, we are no longer in the vacuum limit ($R_1 \gg 1$ but T_0 is not). Thus, the mode shape is not a simple sinusoidal function of the form Eq. (34), but the waviness still increases with decreasing T_0 for heavy membranes.

We now consider the changes in the eigenvalues and associated eigenmode shapes as we pass through the stability boundary for a fixed mass density, the fixed-free analog of Fig. 6. In Fig. 10, the colors label $Y'_{\rm RMS}$, given by Eq. (32). For the larger R_1, 1000 [Fig. 10(a)] the unstable modes are odd-numbered and they become unstable in order of increasing n. The third mode becomes unstable first, at $T_0 \approx 10^{1.36}$—consistent with Fig. 9. Then the fifth mode ($n = 5$) becomes unstable at $T_0 \approx 10^{1.33}$, the seventh mode at $T_0 \approx 10^{1.24}$, and the ninth mode at $T_0 \approx 10^{1.18}$. The even-numbered modes and the first mode remain stable for all values of T_0. Contrary to the fixed-fixed case with $R_1 = 1000$ [Fig. 6(a)] where the four branches with the largest positive $\sigma_{\rm I}$ correspond to modes $n =$

1, 3, 5, 7, the branches with largest σ_I in the fixed-free case correspond to modes $n = 1, 2, 4, 6, 8$. This additional branch with opposite parity ($n = 1$) in Fig. 10(a) has a slightly smaller σ_I than the second mode at the smallest $T_0 = 10^1$ shown. Above a certain T_0 value, the $n = 1$ branch acquires the largest $\sigma_I > 0$.

We show the membrane shapes of the nine lowest wave-number modes to the left of Fig. 10(a) at the lowest $T_0 = 10^1$, but also examples of membrane shapes at a couple of larger T_0 values for the first two unstable branches and observe that the mode shapes are almost unchanged. The Y'_{RMS} values that correspond to these nine lowest wave-number modes are approximately those of the analytical eigenmodes in Eq. (34), $(n - 1/2)\pi/2$ for $n = 1, 2, \ldots, 9$. Even though higher wave-number shapes (yellow dots) appear to become unstable at a larger T_0 value, such cases are not numerically resolved and are thus not used in determining T_{0C} here. At $R_1 = 1000$, the branches with the largest $\sigma_I > 0$ are all continuous but, at $R_1 = 10$, the same branches [blue dots at the top of Fig. 10(c) and bottom of Fig. 10(d)] are more scattered. There, the numerical method gives individual eigenvalues that do not seem to follow a particular branch, as was also found for fixed-fixed membranes at $R_1 = 10$. This could potentially be due to our choice for the range and density of the mesh of initial eigenvalue guesses. The loss of stability in Fig. 10(c) occurs at $T_0 \approx 10^{0.26}$. The imaginary parts of the eigenvalues [Fig. 10(c)] are about two orders of magnitude higher than in Fig. 10(a). At $R_1 = 10$, we see four branches that fall below $\sigma_I = 0$, each having approximately its own distinct value of Y'_{RMS}. If we consider smaller values of T_0, we would expect to observe more branches becoming unstable. As opposed to Fig. 10(a), we see in Fig. 10(c) that the yellow dots (higher wave-number modes) are mostly stable. Similar to the fixed-fixed case in Fig. 6, we see that the curves connecting the σ_R associated with a particular mode shape appear to be steeper in Fig. 10(d) than in Fig. 10(b).

In summary, the fixed-free stability boundary is lower than the fixed-fixed boundary at small and moderate values of R_1—so more membranes are stable—but resembles the upward-sloping portion of the fixed-fixed boundary at large R_1 ($\geqslant 10^2$). Similarly to fixed-fixed membranes (Sec. IV), when R_1 and T_0 dominate fluid pressure forces the eigenmodes tend to neutrally stable sinusoidal functions with odd-numbered modes becoming unstable, starting with the third mode. We find that in the small R_1 region (i.e., $R_1 < 10^{-1}$) the most unstable eigenmodes have a small deflection at the trailing edge, despite its freedom to move in the vertical direction. The small-R_1 modes are very wavy shapes. For all R_1, the modes become wavier with decreasing T_0. At moderate and large R_1, the waves are superposed on a background shape with nonzero slope.

VI. FREE-FREE MEMBRANES

We have found that allowing the trailing edge to deflect freely in the vertical direction dramatically changes the instability region and the membrane dynamics. As a natural next step, we now study the effect of making both ends free, satisfying the boundary conditions Eq. (13). The stability boundary (red line) and most unstable eigenvalues are shown in Fig. 11. The stability boundary is similar to the fixed-free case (Fig. 7): the critical pretension increases with mass when $R_1 > 10^2$, it decreases as we decrease R_1, and it plateaus when $R_1 \ll 1$. In Fig. 11, we show that there is close agreement for $R_1 \in [10^{-0.75}, 10^{0.5}]$ between the stability boundary computed here and in Ref. [1] using unsteady simulations (orange line). For smaller R_1 ([$10^{-3}, 10^{-1}$]) and larger R_1 ([$10^{0.75}, 10^2$]), the red line has slightly higher T_0. As noted in Sec. V, the difference in m (40 in Ref. [1] versus 120 here) may be the main cause. As for the fixed-free case, we will show that the most unstable eigenmodes have higher wave numbers at the smallest R_1, so numerical resolution is an issue there: In Ref. [1], we found that the small- and large-amplitude motions were not converged with $m = 40$ for $R_1 < 10^{-1}$.

We can again use the imaginary [Fig. 11(a)] and real parts [Fig. 11(b)] of the eigenvalues to characterize the instability in (R_1, T_0) space. Within the region of instability (below the red line), a comparison with fixed-fixed (Fig. 4) and fixed-free membranes (Fig. 7) reveals that the colored dots (most unstable eigenvalues) have the same general behavior: the temporal growth rates [Fig. 11(a)]
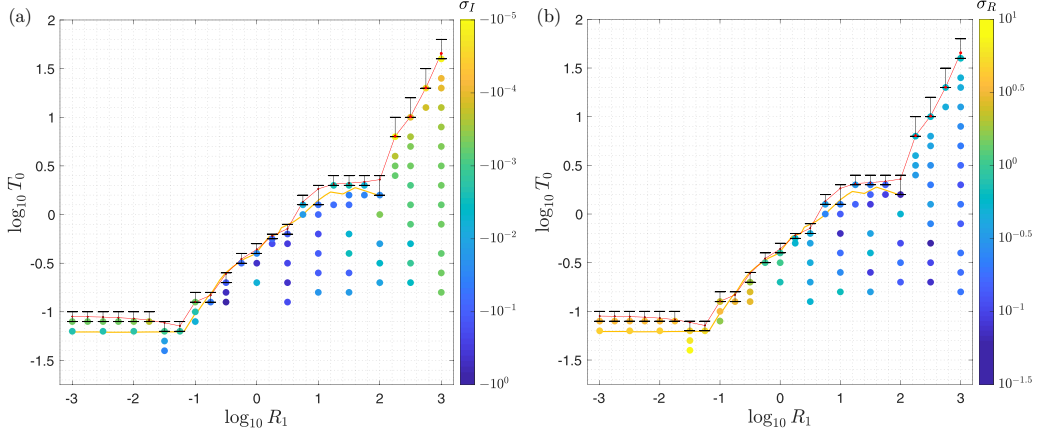
FIG. 11. The region in R_1–T_0 space in which the free-free membrane is unstable. The red line and red dots indicate the position of the stability boundary computed using linear interpolation between σ_I of the smallest T_0 that gives a stable membrane and the σ_I of the largest T_0 that gives an unstable membrane (shown in the error bars). The color of the dots below the stability boundary labels: (a) The imaginary part of the eigenvalue (σ_I) corresponding to the most unstable modes. It represents the temporal growth rate. (b) The real part of the eigenvalues (σ_R) for the most unstable mode, representing the angular frequency. The orange line that spans $R_1 \in [10^{-3}, 10^2]$ represents the stability boundary computed numerically in Ref. [1].

increase in magnitude with decreasing R_1 and T_0, but vary nonmonotonically with T_0 at moderate values of R_1 ($[10^0, 10^2]$). The growth rates of free-free heavy membranes ($R_1 \in [10^2, 10^3]$) are qualitatively similar to those in the fixed-free case in the same region. The angular frequencies (σ_R, Fig. 11(b)) are also larger for smaller R_1, but vary nonmonotonically with T_0. Similar to the fixed-free case, we observe that membranes exhibit the flutter and divergence instability but do not lose stability solely by divergence (i.e., with $\sigma_R \approx 0$) for any (R_1, T_0) pair. In the region $R_1 \lesssim 10^{-1.25}$,
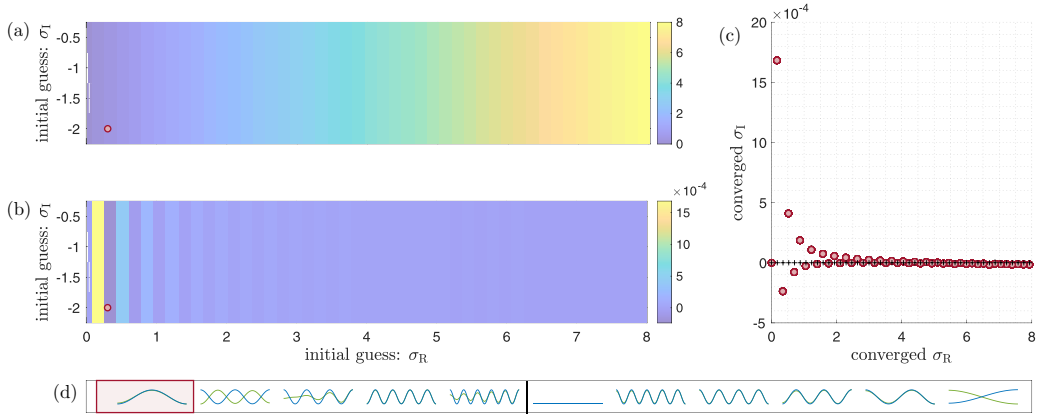

FIG. 12. Free-free eigenvalues and eigenmodes with $R_1 = 10^3$ and $T_0 = 10^{1.1}$. Computed σ_R [(a), values in color bars at right] and computed σ_I [(b), values in color bars at right], both plotted in the initial guess complex plane. (c) The distinct eigenvalues generated by the numerical method plotted as red dots in the (σ_R, σ_I) plane. The analytical form of the eigenvalues is $\sigma = ((n-1)\pi/2)\sqrt{T_0/R_1}$ for $n = 1, \ldots, 46$ (black pluses). (d) The 11 lowest wave-number eigenmodes [$\text{Re}(Y(x))$ in green, $\text{Im}(Y(x))$ in blue], from the most unstable (most negative σ_I) on the left to the most stable (largest positive σ_I) on the right. The vertical black line separates unstable modes (on its left) and stable modes (on its right).
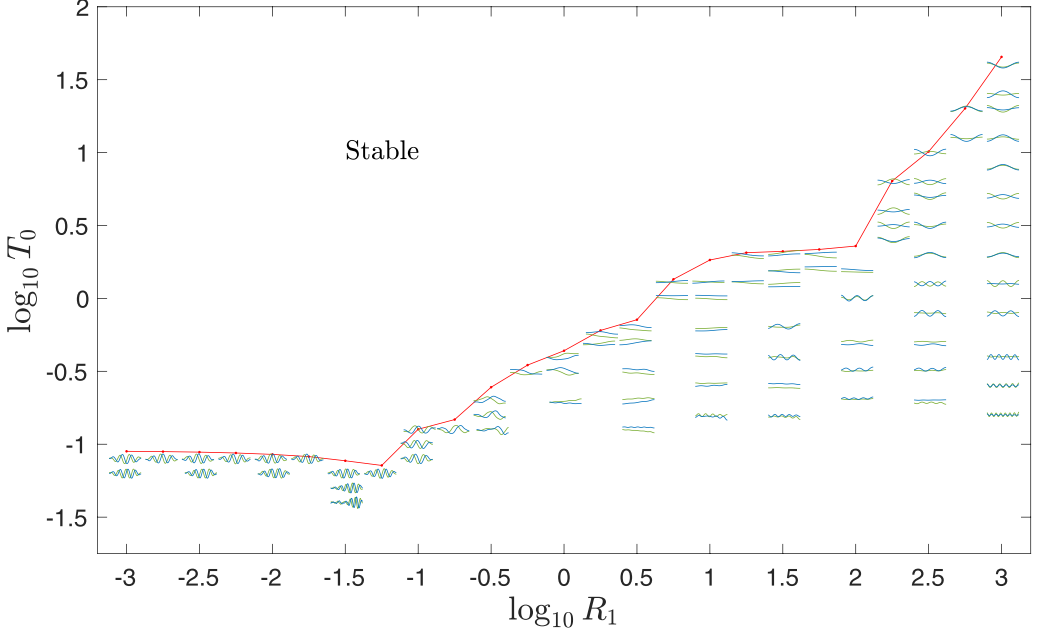
FIG. 13. The shapes $Y(x)$ of the most unstable eigenmode as a function of R_1 and T_0 in the free-free case. The real part of $Y(x)$ is shown in green and the imaginary part of $Y(x)$ is shown in blue. Each shape is scaled, both vertically and horizontally, to fit within the plot. The shapes are superposed on the same stability boundary (red line) as in Fig. 11.

the eigenvalues just below the stability boundary are nearly constant; observed also in the fixed-free case (Fig. 7).

For $R_1, T_0 \gg 1$, the eigenvalues are the same as for the fixed-fixed case Eq. (30), with the addition of zero. The free-free eigenmodes are given by

$$Y(x) = \cos\left(\frac{(n-1)\pi}{2}(x+1)\right) \tag{35}$$

for $n \in \mathbb{Z}_{>0}$ and $-1 \leqslant x \leqslant 1$, where the amplitude is arbitrary.

Figure 12 shows an example of how the computed eigenvalues [real parts in Fig. 12(a) and imaginary parts in Fig. 12(b)] vary over a grid of initial guesses in the complex plane for a free-free membrane with $R_1 = 10^3$ and $T_0 = 10^{1.1}$, with the same mesh as in the fixed-free case of Fig. 8. We take R_1 and $T_0 \gg 1$ (vacuum limit) to compare with the analytical values Eq. (30) with $k = (n-1)\pi/2$ for $n \in \mathbb{Z}_{>0}$ [Fig. 12(c)]. In Fig. 12(d), we show the 11 lowest wave-number modes. Starting from the left, the most unstable modes are $n = 3, 5, 7, 9,$ and 11 whereas $n = 1, 10, 8, 6, 4,$ and 2 are stable. The sixth shape from the left that is displayed is flat ($n = 1$), with corresponding σ_R and $\sigma_I \approx 10^{-8}$.

In Fig. 13, we show the most unstable eigenmodes across (R_1, T_0) space. The mode shapes of light membranes ($R_1 \leqslant 10^{-1.75}$) just below the stability boundary seem very similar to fixed-free membranes with the same mass but have one less peak and one less trough. Decreasing the pretension values for membranes with $R_1 \leqslant 10^{-1.5}$ not only makes the membrane profile more wavy but also causes the ripples in the membrane shape to move rearward to the trailing edge. Mode shapes with nearly zero deflection at the free ends exist up to $R_1 = 10^{-0.75}$, slightly higher than in the fixed-free case (Fig. 9). When the mass density is between $10^{0.75}$ and 10^2 and the pretension is between 10^0 and $T_{0C}(R_1)$, the membranes are somewhat straighter than in the fixed-free case.
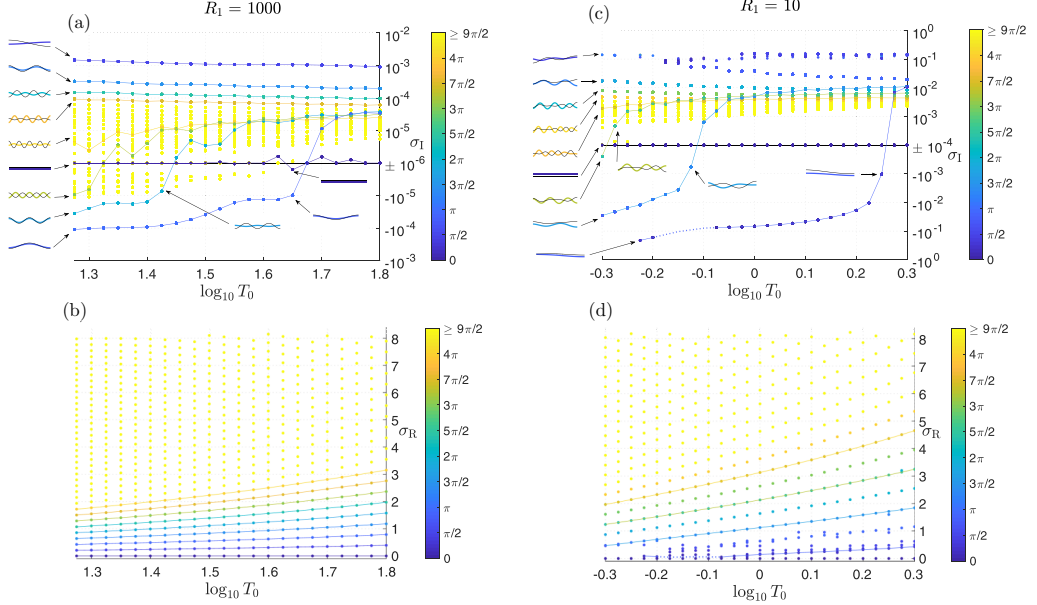
FIG. 14. For two values of membrane mass (R_1), 10^3 (left column) and 10^1 (right column), the imaginary [(a), (c)] and real parts [(b), (d)] of the eigenvalues versus pretension (T_0) for free-free membranes. Numerical results are shown as points with color coded according to the value of the RMS of the membrane's slope for each (R_1, T_0) pair given by Eq. (32), as given in the color bar. The horizontal black line in the top panels located at (a) $\sigma_I = \pm 10^{-6}$, (c) $\sigma_I = \pm 10^{-4}$ distinguishes stable modes (above) and unstable modes (below). We also show typical modes that correspond to each branch with $Y'_{RMS} < 9\pi/2$.

Finally, heavy membranes ($R_1 > 10^2$) with T_0 between $10^{0.3}$ and $T_{0C}(R_1)$ (the stability boundary) all lose stability with the third mode, $n = 3$ in Eq. (35) [the highlighted mode in Fig. 12(d)].

In Fig. 11, we studied how the most unstable eigenvalues change in the R_1–T_0 parameter space, and in Fig. 13 we investigated the trends in the corresponding most unstable eigenmodes. Now in Fig. 14 we show the changes in the eigenvalues and associated eigenmode shapes as we pass through the stability boundary for two fixed values of mass density, as for the fixed-fixed and fixed-free cases (Figs. 6 and 10, respectively). Each dot's color is used to label Y'_{RMS} [Eq. (32)]. For the largest $R_1 = 1000$ [Fig. 14(a)] the unstable modes are odd-numbered. The first branch to become unstable is the third mode [$n = 3$ in Eq. (35)] at $T_0 \approx 10^{1.68}$—consistent with Fig. 13 (for the same R_1). Then the fifth mode ($n = 5$) becomes unstable at $T_0 \approx 10^{1.45}$ and the seventh mode at $T_0 \approx 10^{1.33}$. The even-numbered modes are all stable for the entire range of T_0 values considered here. We show the membrane mode shapes that correspond to the nine lowest wave-number modes to the left of Fig. 14(a) at the lowest $T_0 = 10^{1.275}$. The Y'_{RMS} values that correspond to these nine lowest wave-number modes are approximately those of the analytical eigenmodes in Eq. (35), $(n-1)\pi/2$ for $n = 1, 2, \ldots, 9$. We also show instances of membrane shapes at a couple of larger T_0 values for the first two unstable branches and the flat mode. We see that in all cases, these mode shapes have the same features as at the smallest T_0. The branch corresponding to the flat mode ($n = 1$) in Fig. 14(a) oscillates about $\sigma_I = \pm 10^{-6}$ at $T_0 \geqslant 10^{1.6}$ (while σ_R lies on $\pm 10^{-4}$)—it is essentially zero. As in the fixed-fixed and fixed-free cases at $R_1 = 1000$, the branches with the largest $\sigma_I > 0$ are all continuous but at the smaller R_1 (i.e., 10), the same branches [blue dots at the top of Fig. 14(c) and bottom of Fig. 14(d)] appear more disordered. The loss of stability in Fig. 14(c) occurs at $T_0 \approx 10^{0.275}$. The values of σ_I in Fig. 14(c) are about two orders of magnitude higher than those in Fig. 14(a) (as for fixed-free membranes at the same membrane masses). The downward tendency of the darker orange
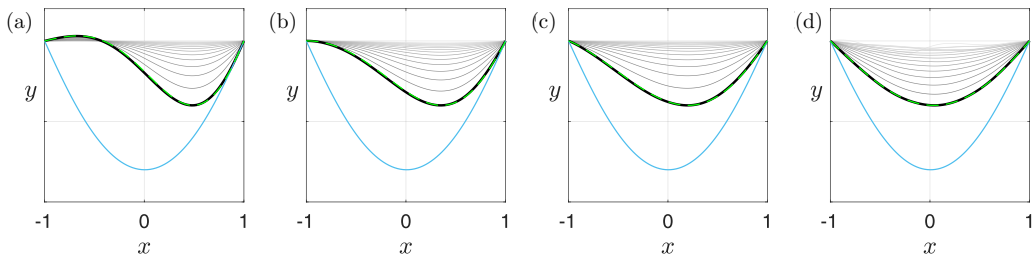
FIG. 15. Fixed-fixed membranes at $R_1 = 10^{-1}$ and (a) $T_0 = 10^{-0.1}$, (b) $T_0 = 10^0$, (c) $T_0 = 10^{0.1}$, and (d) $T_0 = 10^{0.2}$. These membranes lose stability by divergence. We compare the most unstable modes obtained from the eigenvalue analysis (dashed green lines) to the membrane shapes of the time-stepping simulations in the small-amplitude (growth) regime—in each panel, 15 equally spaced snapshots are shown in the growth regime, gray and then black at the last time. The arbitrary amplitudes of the green lines are set to match those of the black lines. The light blue curves indicate shapes in the large-amplitude steady state regime.

branch when σ_I drops below 10^{-2} [Fig. 14(c)] suggests that the mode may be the next to become unstable as T_0 decreases. Contrary to Fig. 14(a), we see in Fig. 14(c) that the yellow dots (higher wave-number modes) are mostly stable. The free-free angular frequency (σ_R) behaves similarly to fixed-fixed and fixed-free membranes: the curves connecting σ_R associated with particular modes are steeper for $R_1 = 10$ [Fig. 14(d)] compared to $R_1 = 1000$ [Fig. 14(b)]. The dotted part of the most unstable branch shown in Figs. 14(c) and 14(d) is used to bridge a gap in T_0 in which we did not find eigenvalues and eigenmodes for the lowest branch.

VII. COMPARISON WITH UNSTEADY AND LARGE-AMPLITUDE SIMULATIONS

We now compare the most unstable eigenmodes, in a few cases, with the corresponding small-amplitude motions as well as the eventual large-amplitude steady-state motions in the unsteady time-stepping simulations of Ref. [1]. The main differences are that in the eigenvalue problem the free vortex wake has a finite length ℓ_w whereas in the unsteady simulations it grows from zero length, and has δ smoothing to avoid chaotic dynamics. For fixed-fixed membranes, Fig. 15 compares eigenmodes (dashed green lines) with snapshots of time-stepping simulations in the small-amplitude growth regime (sequence of gray lines ending with black lines) and the time-stepping simulations' eventual large-amplitude steady states (blue lines). The comparison is made at $R_1 = 10^{-1}$ with T_0 increasing: (a) $10^{-0.1}$, (b) 10^0, (c) $10^{0.1}$, and (d) $10^{0.2}$, the last value close to the stability boundary. Here we have a divergence instability, so the imaginary parts of the eigenmodes are zero; the green lines show the real parts. As T_0 increases, the small-amplitude membrane shapes change gradually, from ones with both downward and upward curvature [Fig. 15(a)] to a nearly fore-aft symmetric hump with upward curvature only [Fig. 15(d)]. The close agreement between the green and black lines shows that the linearized model captures the small-amplitude unsteady dynamics well. Here the initial deflection is $y(x, 0) = 10^{-12} \sin(\pi x)$, but we find essentially the same agreement with a different form of the initial perturbation, in which the leading edge is moved slightly upward and then back to $y = 0$. In this case, the membrane initially forms a small bump near the trailing edge as it evolves under the nonlinear membrane Eq. (5). Both types of initial deflections are much smaller than the gray shapes in Fig. 15, and eventually converge to them as the fastest growing mode outgrows the other modal components of the initial deflections. At large times, all the unsteady shapes converge to steady humps (blue lines), nearly fore-aft symmetric, despite the early-time differences. The magnitudes of the humps' deflections are set by the nonlinear stretching resistance in Eq. (5), the term proportional to the stretching modulus R_3. Here R_3 is set to 10 but only the magnitudes of the humps, and not their shapes, change much over the range $R_3 \geqslant 10$ [1].

We now investigate membranes with the leading edges fixed and the trailing edges free. Now the membranes lose stability through divergence and flutter, so the eigenmodes are complex. They
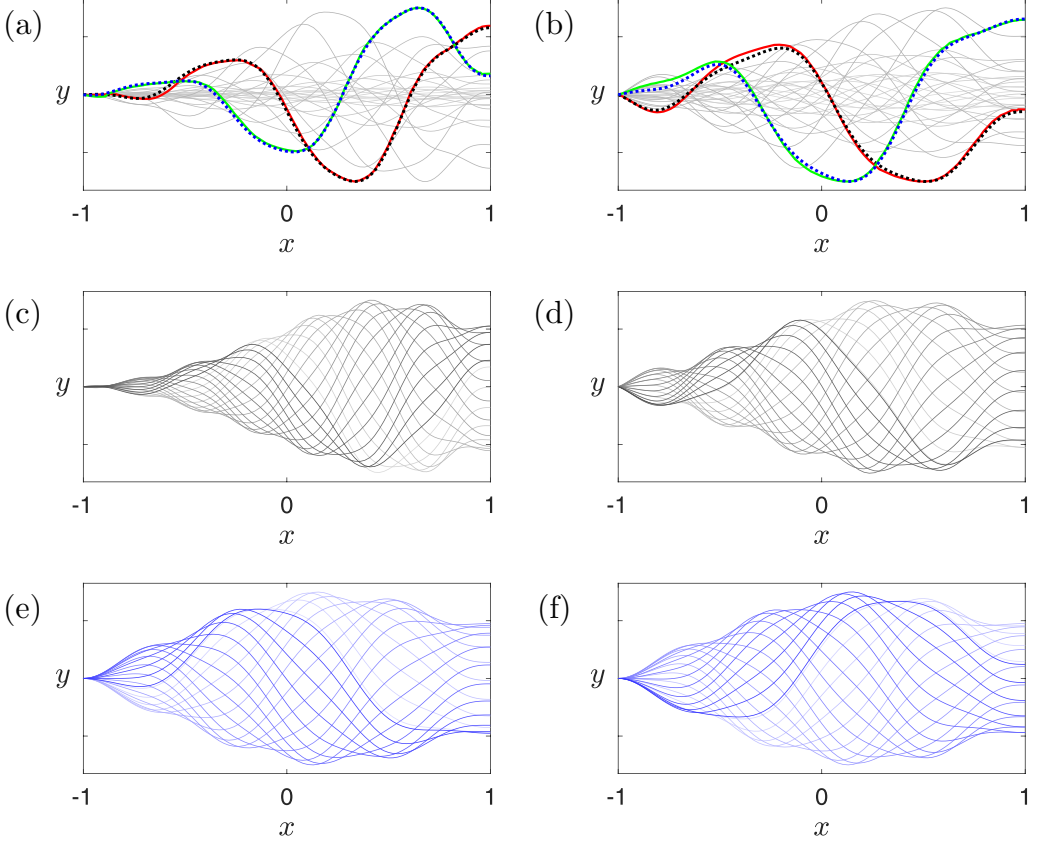
FIG. 16. Fixed-free membranes at $R_1 = 10^{-0.5}$ and $R_3 = 10^{1.5}$, with $T_0 = 10^{-0.8}$ for (a), (c), (e) and $T_0 = 10^{-0.7}$ for (b), (d), (f). In (a) and (b), the solid red lines are $\text{Re}(y_{\text{nonlin}}(\alpha))$ estimated from the time-stepping simulation, which are close to $\text{Re}(Y(x))$ from the eigenvalue problem (dotted black lines). The solid green lines are $\text{Im}(y_{\text{nonlin}}(\alpha))$, close to $\text{Im}(Y(x))$ from the eigenvalue problem (dotted blue lines). The gray lines are a subset of snapshots in the linear growth regime. In (c) and (d), we show snapshots during the small-amplitude (growth) regime, but with the exponential growth removed. (e), (f) show snapshots during the steady-state large-amplitude motions. We show 20 equally spaced snapshots of membranes over a period, ranging from light blue at earlier times to dark blue at the last time.

are determined only up to a complex constant, with both a magnitude and a phase that need to be matched to a given time-stepping simulation of Ref. [1]. In Appendix B, we give details about how the matching is done.

In Fig. 16, we compare two cases slightly below the stability boundary at $R_1 = 10^{-0.5}$: $T_0 = 10^{-0.8}$ [Figs. 16(a), 16(c) 16(e)] and $T_0 = 10^{-0.7}$ [Figs. 16(b), 16(d) and 16(f)]. In Figs. 16(a) and 16(b), the gray lines again show sequences of snapshots from the time-stepping simulations. We fit the values $y(\alpha, t)$ for such a sequence to a function of the form $\text{Re}([\text{Re}(y_{\text{nonlin}}(\alpha)) + i\text{Im}(y_{\text{nonlin}}(\alpha))]e^{i\sigma t})$. First, σ_I and σ_R are estimated. Then for each α, the real and imaginary parts of $y(\alpha, t)e^{-i\sigma t}$ are estimated (in amplitude-phase form; see Appendix B), giving $\text{Re}(y_{\text{nonlin}}(\alpha))$ [red solid lines in Figs. 16(a) and 16(b)] and $\text{Im}(y_{\text{nonlin}}(\alpha))$ (green solid lines). The most unstable eigenmode $Y(x)$ is arbitrary up to a complex constant. The function $y_{\text{nonlin}}(\alpha)$ contains a complex factor (magnitude and phase) that depends on the initial conditions of the time-stepping simulation. To account for this, we scale $Y(x)$ by the complex factor that gives the best L^1-fit with $y_{\text{nonlin}}(\alpha) \approx y_{\text{nonlin}}(x)$ (see Appendix B) and plot the resulting $\text{Re}(Y)$ and $\text{Im}(Y)$ as dotted black and
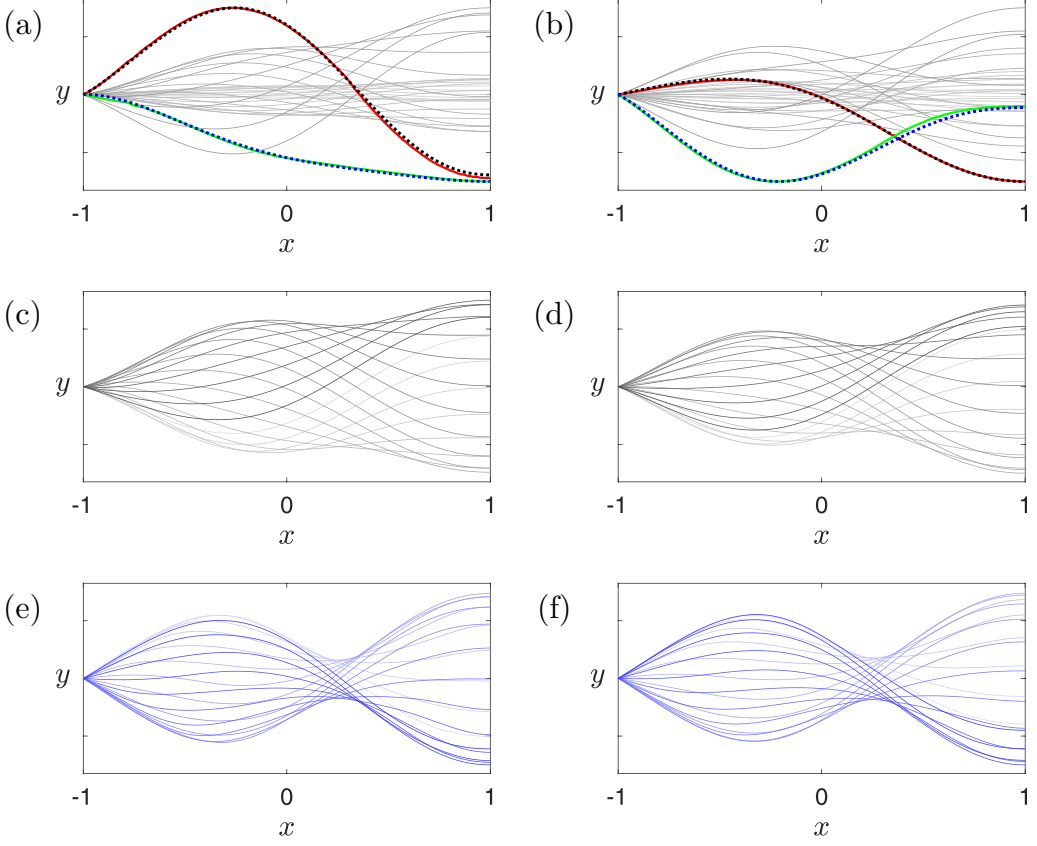
FIG. 17. Same quantities as described in Fig. 16 but with $R_1 = 10^1$ and $R_3 = 10^{1.5}$, and $T_0 = 10^{-0.1}$ [for (a), (c), and (e)]; $T_0 = 10^0$ [for (b), (d) and (f)].

blue lines respectively, in Figs. 16(a) and 16(b). The fit between $Y(x)$ and $y_{\mathrm{nonlin}}(x)$ is nearly as good as in the steady fixed-fixed cases (Fig. 15). The slight increase of error in the fit may be due to the extra steps involved in fitting the fixed-free eigenmodes because they are complex.

In Figs. 16(c) and 16(d), we show 20 snapshots from the time-stepping simulations, but multiplied by our estimate of $e^{\sigma_I t}$, which should remove the exponential growth. This shows the mode shapes much more clearly than in Figs. 16(a) and 16(b). The rescaled shapes are equally spaced over our estimate of one time period. They appear to follow an up-down symmetric, periodic (as expected) oscillation with seven [Fig. 16(c)] and five [Fig. 16(d)] "necks" in their envelopes, respectively. Figs. 16(e) and 16(f) show snapshots in the eventual large-amplitude periodic steady-state. The shapes are qualitatively similar to those in Figs. 16(c) and 16(d), but the numbers of necks are reduced to four in both Figs. 16(e) and 16(f). The shapes are nearly the same in both panels; as in the fixed-fixed case (Fig. 15) the differences in the small-amplitude shapes disappear at large amplitude. This may be because the T_0 term in Eq. (5) is subdominant to the R_3 term at large amplitudes, even at $T_{0C}(R_1)$, the largest T_0 where the membranes are unstable.

We show the same comparisons at larger R_1 (10) in Fig. 17 at two T_0 values near the stability boundary. The wave numbers of the shapes are much reduced—only one neck appears in each envelope now—but otherwise many of the same features carry over from the previous figure. There is again good agreement between the eigenmodes and the versions estimated from the time-stepping simulations [Figs. 17(a) and 17(b)]. The periodic parts of the small-amplitude motions have small but noticeable differences in Figs. 17(c) and 17(d)—in particular, the widths of the necks relative

to the maximum widths of the envelopes. The large-amplitude motions [Figs. 17(e) and 17(f)] are again nearly indistinguishable, however.

We obtain similar levels of agreement in the free-free case; two examples are shown in Appendix C.

VIII. CONCLUSIONS

To summarize, we have used a linearized model and a nonlinear eigenvalue solver to study small amplitude membrane motions, including the onset of membrane instability, in inviscid fluid flows. We characterized the different types of possible motions with respect to the two key dimensionless parameters—membrane mass and pretension—and for three sets of boundary conditions: fixed-fixed, fixed-free, and free-free leading and trailing edges. Previous work by other groups was limited to the fixed-fixed case and a smaller range of membrane mass densities, and our own previous time-stepping simulations [1] were unable to resolve the small-amplitude motions at small mass densities due to limited spatial resolution and at large mass densities due to the very slow growth of instabilities.

For each of the three sets of boundary conditions, when membrane inertia and pretension dominate fluid pressure forces, the eigenmodes tend toward neutrally stable sinusoidal functions with half-integer or quarter-integer numbers of wavelengths. When the fluid forces are small but nonnegligible, the mode shapes are similar, but the even- (for fixed-fixed) or odd-numbered modes (for fixed-free and free-free) become unstable, starting with the second and third modes, respectively. For the fixed-fixed case, there are roughly two regimes: small membrane density, where divergence occurs and the most unstable mode becomes more fore-aft asymmetric as one moves further into the instability region, and large membrane density, where flutter and divergence occur with approximately sinusoidal modes. In both regimes, the most unstable modes become wavier at smaller T_0, akin to the most unstable beam modes at smaller bending rigidity in Ref. [37]. These results agree with those of Ref. [3] in the same parameter regimes.

The stability boundaries for the fixed-free and free-free cases resemble the fixed-fixed case at large membrane densities, showing an upward slope for $R_1 \geqslant 10^2$ (which we were not able to compute using time-stepping simulations). The fixed-free and free-free stability boundaries differ strongly from the fixed-fixed case at moderate and small membrane densities. There the membranes remain stable down to smaller pretension values, and eventually become unstable by flutter and divergence. For $10^{-3} \leqslant R_1 \leqslant 10^{-1}$, the most unstable mode is very wavy, and we were unable to resolve it with the time-stepping simulations in Ref. [1]. Here we find that the most unstable eigenmodes have small deflection at the leading and trailing edges, despite the free boundary conditions. For $10^{-1} \leqslant R_1 \leqslant 10^2$, the modes are wavy shapes (wavier at smaller T_0) superposed on background shapes with nonzero slopes (fixed-free) and/or deflections (free-free). By tracking the eigenmodes across the stability boundaries, we found that at moderate membrane densities, the modes resemble the sinusoidal shapes at large densities but with more disorder and the appearance of irregular bands of stable low-wave-number modes that are difficult to associate with a particular branch.

Finally, we compared the eigenmodes with the membrane motions in the time-stepping simulations and found very good agreement with the small-amplitude portion of the time-stepping simulations in examples with the three different boundary conditions. In all the examples, the large-amplitude motions qualitatively resembled those in the small amplitude regime in terms of the number of necks in the deflection envelopes, but had clear differences in the envelopes' shapes and the relative sizes of maxima and minima.

APPENDIX A: CONVERGENCE WITH RESPECT TO NUMBER OF CHEBYSHEV NODES

In this paper, we have computed the membrane eigenmodes and eigenvalues using $m = 120$ (121 Chebyshev points on the membrane) and a free vortex wake of length $\ell_w = 39$. We consider here the effect of varying the former. The effect of varying the vortex wake length was explored in Ref. [[37], Sec. V], and here we find that the results in the unstable regime are basically unchanged when ℓ_w is as large as 39, given the exponential decay of circulation in the wake (except right on the stability boundary, but there is still algebraic decay of the induced velocity by an alternating-sign wake).

To compare the eigenmodes obtained when using $m = 80$ versus 120, we remove the arbitrary phase shift from the eigenmode solver by finding $\phi \in [0, 2\pi]$ that solves

$$\min_{\phi} \int_{-1}^{1} |Y_{80}(x) - Y_{120}(x)e^{i\phi}| \, dx. \tag{A1}$$

To perform the subtraction in Eq. (A1), we interpolate Y_{80} using shape-preserving piecewise cubic interpolation onto the 120-point grid. In Fig. 18, we compare the real [Fig. 18(a)] and imaginary parts [Fig. 18(b)] of the fixed-free eigenmodes when using $m = 80$ and 120 across an array of (R_1, T_0) pairs. The eigenmodes agree well except in some cases at the smallest values of T_0 for each R_1, where the modes are also more wavy and difficult to resolve numerically. In Fig. 19, we present the relative error in the eigenvalues when $m = 80$ and 120. This quantity is computed as

$$\text{relative error} = \left| \frac{\sigma_{80} - \sigma_{120}}{\sigma_{120}} \right|. \tag{A2}$$

The errors are typically 10^{-2}–10^{-5} near the stability boundary, and gradually increase to 10^{-1}–10^0 as we decrease T_0, eventually reaching a point where the solutions are under-resolved (as in Fig. 18).

Figure 20 shows three examples of the computed eigenvalues using grids of initial guesses with $m = 80$ (green diamonds), 120 (red circles), and 240 (blue crosses). Figure 20(a) corresponds to a fixed-free membrane at a moderate value of R_1 ($10^{0.5}$) and $T_0 = 10^{-0.25}$. The eigenvalues agree well except for an additional stable eigenmode found when $m = 240$ [small blue cross located at $(\sigma_R, \sigma_I) \approx (0.29, 0.13)$]. Figure 20(b) corresponds to a fixed-free membrane with a larger value of R_1 (10^3), and $T_0 = 10^{0.8}$. The eigenvalues agree well at the three values of m when $\sigma_R \lesssim 2.5$, approximately the 15 lowest modes. As σ_R increases, the modes are eventually under-resolved and the eigenvalues deviate significantly, beginning with $m = 80$ (green diamonds). Figure 20(c) corresponds to a free-free membrane at $R_1 = 10^{0.5}$ as in Fig. 20(a) but with T_0 slightly smaller, $10^{-0.5}$. As in Fig. 20(a), there are extra stable eigenvalues (with $\sigma_R < 2$ and $\sigma_I > 0.1$), most with $m = 240$ (blue crosses) and one with $m = 80$ (green diamond). These eigenvalues are similar to those in the irregular bands of stable eigenvalues in Figs. 6, 10, and 14 when $R_1 = 10$. We have good agreement among the eigenvalues that are unstable or close to neutrally stable. In each case, the most unstable modes (i.e., the modes associated with smallest—or most negative—σ_I) change little when m increases from 120 to 240, and they are the focus of this paper.

APPENDIX B: METHOD FOR COMPARING THE EIGENVALUE ANALYSIS RESULTS TO TIME-STEPPING SIMULATIONS

Here we outline the method for comparing mode shapes obtained using the eigenvalue analysis developed in the current paper and mode shapes obtained from the time-stepping simulations in Ref. [1].

We first determine the regime of exponential growth in the nonlinear simulations by plotting the trailing edge deflection as a function of time, i.e., $y(1, t)$. The time it takes to reach the large-amplitude steady-state regime depends on the magnitude of the initial perturbation. To extend the time spent in the small-amplitude regime, we start with a very small perturbation, $O(10^{-12})$. This is
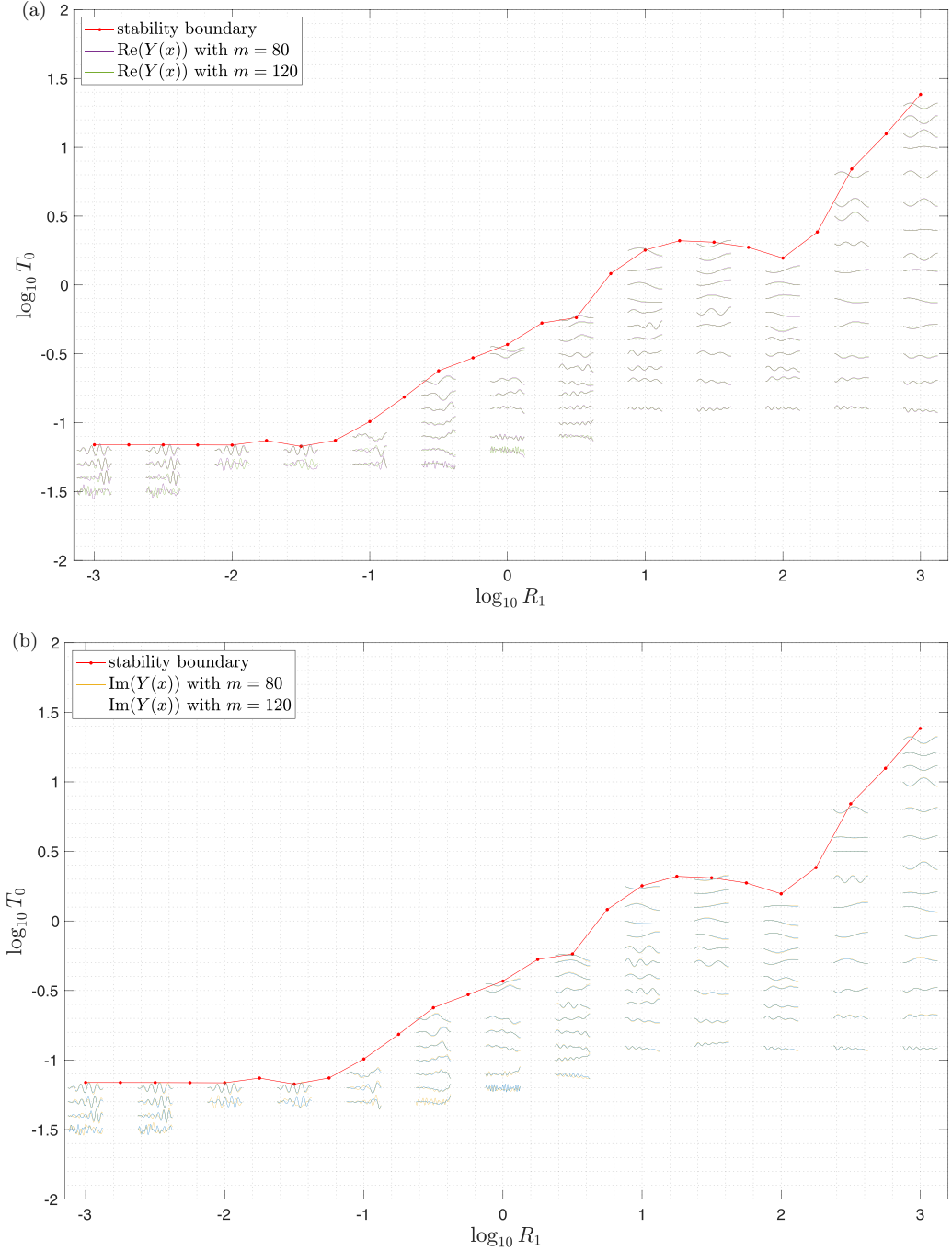
FIG. 18. Comparison between the (a) real and (b) imaginary parts of the eigenmodes with fixed-free boundary conditions, using grids with $m = 80$ and $m = 120$. Each shape is scaled in both vertical and horizontal directions to fit within the plot. The red dots indicate the position of the stability boundary (same as in Fig. 9).
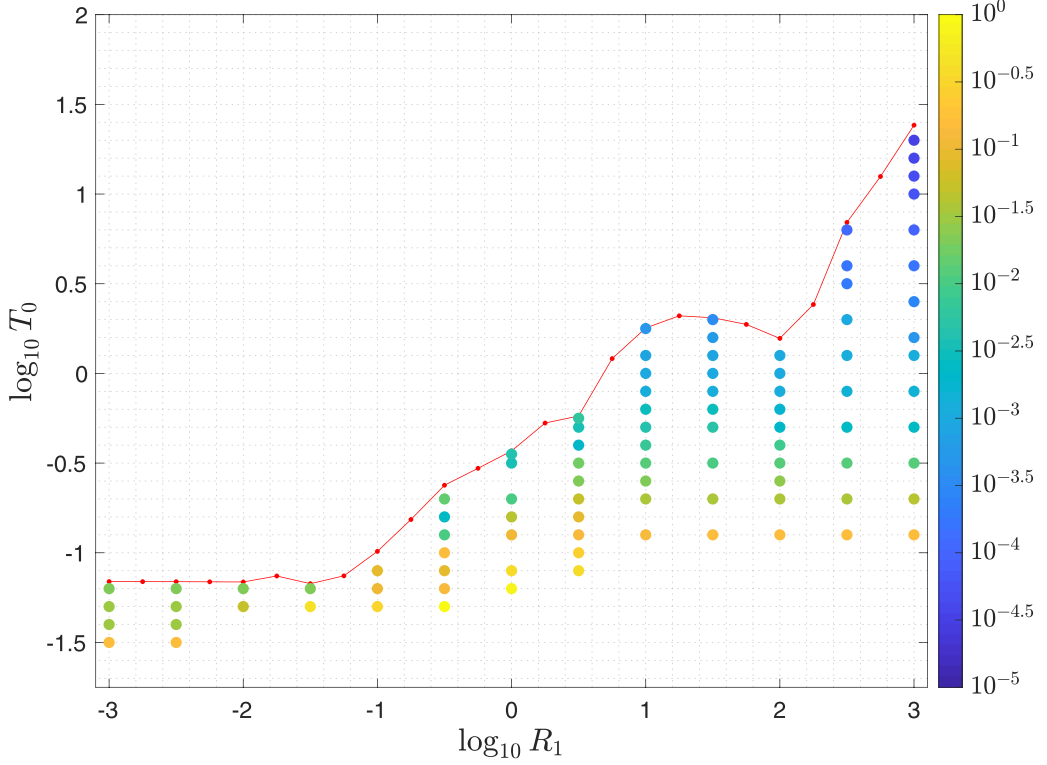
FIG. 19. At each (R_1, T_0) in the instability region (below red line), the relative error Eq. (A2) in the eigenvalues when using $m = 80$ and $m = 120$ Chebyshev points on the fixed-free membrane is plotted as a colored dot.

important particularly when the growth rate is large, i.e., for unstable membranes that are far from the stability boundary in parameter space.

During this exponential growth (with flutter) regime, we approximate the computed $y(\alpha, t)$ as

$$y(\alpha, t) \approx \text{Re}([\text{Re}(y_{\text{nonlin}}(\alpha)) + i\text{Im}(y_{\text{nonlin}}(\alpha))]e^{i\sigma t}). \tag{B1}$$

To obtain σ and $y_{\text{nonlin}}(\alpha)$, we first obtain σ_{I} as the negative of the slope of $\ln(|y|)$ versus time [Fig. 21(a)] and subsequently compute $y(\alpha, t)e^{\sigma_{\text{I}}t}$. For each grid point $1, \dots, m + 1$ in $\alpha \in [-1, 1]$, this is a function that oscillates sinusoidally in time but does not grow [Fig. 21(b)].
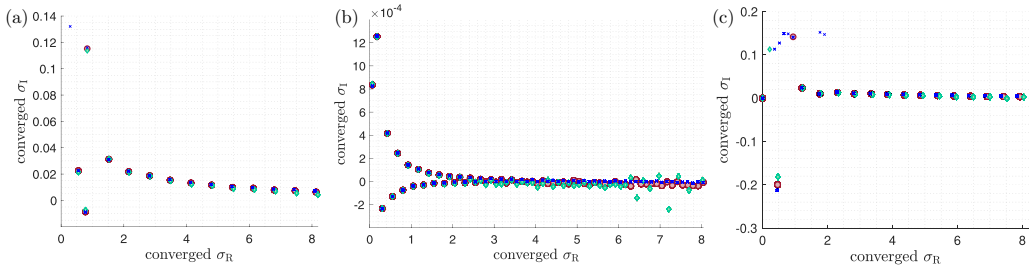

FIG. 20. Spectrum of eigenvalues for $m = 80$ (green diamonds), 120 (red circles), and 240 (blue crosses) for a fixed-free membrane at (a) $(R_1, T_0) = (10^{0.5}, 10^{-0.25})$, (b) $(R_1, T_0) = (10^3, 10^{0.8})$, and a free-free membrane at (c) $(R_1, T_0) = (10^{0.5}, 10^{-0.5})$.
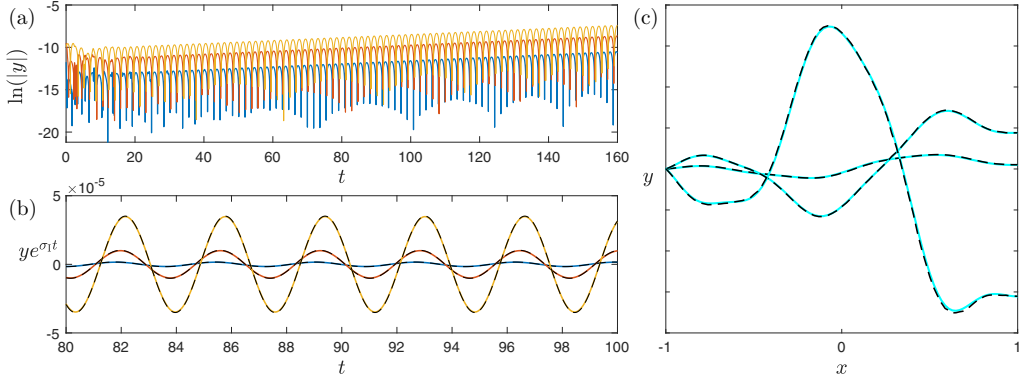
FIG. 21. Example of the comparison method using data from fixed-free membranes with $(R_1, T_0) = (10^{-0.5}, 10^{-0.7})$. (a) $\ln(|y|)$ versus time for the 10th (blue), 30th (red), and 100th (yellow) grid points on the membrane. (b) A portion of the time series of $ye^{\sigma_I t}$ at the 10th (blue), 30th (red), and 100th (yellow) grid points. This corresponds to part of the small-amplitude regime but with the growth removed. The black dashed lines represent the constructed $R(\alpha)\cos(\sigma_R t + \phi(\alpha))$ at the same grid points. (c) The reconstructed data $\text{Re}([\text{Re}(y_{\text{nonlin}}(\alpha)) + i\text{Im}(y_{\text{nonlin}}(\alpha))]e^{i\sigma t})$ (black dashed lines) compared against the data $y(\alpha, t)$ (cyan solid lines) at the times $t = 20, 100, 160$. The initial perturbation here is $\zeta(\alpha, 0) = \eta \sin(\pi\alpha)$ where η is chosen as 0.0001. Note that the axes are not to scale.

We estimate the frequency f of these functions as the reciprocal of the time between the peaks of the sinusoidal function. The frequency should be the same for all $\alpha \in [-1, 1]$ according to our ansatz, and the computed values vary only slightly due to numerical errors. We use the average over α as our estimate of the single, global frequency. We then define $\sigma_R := 2\pi f$ and denote the amplitudes of these sinusoidal functions $R(\alpha)$. We denote by $t_{\text{peak}}(\alpha)$ the times at which they reach their peaks and define the phase as $\phi(\alpha) := -\sigma_R \cdot t_{\text{peak}}(\alpha)$. Thus, we have

$$\text{Re}(y_{\text{nonlin}}(\alpha)) = R(\alpha)\cos(\phi(\alpha)), \tag{B2}$$

$$\text{Im}(y_{\text{nonlin}}(\alpha)) = R(\alpha)\sin(\phi(\alpha)). \tag{B3}$$

We show in Fig. 21(c), the reconstructed data $\text{Re}([\text{Re}(y_{\text{nonlin}}(\alpha)) + i\text{Im}(y_{\text{nonlin}}(\alpha))]e^{i\sigma t})$ (black dashed line) compared to $y(\alpha, t)$ (cyan solid lines) at three times.

Finally, we choose a phase ϕ that gives the best match between $Y(x)$ from the eigenvalue analysis described in Sec. III and $y_{\text{nonlin}}(\alpha)$ from the nonlinear simulations. We do this by solving the following optimization problem:

$$\min_{\phi} \int_{-1}^{1} \left| \frac{[\text{Re}(y_{\text{nonlin}}(x)) + i\text{Im}(y_{\text{nonlin}}(x))]}{\max(|[\text{Re}(y_{\text{nonlin}}(x)) + i\text{Im}(y_{\text{nonlin}}(x))]|)} - \frac{Y(x)e^{i\phi}}{\max(|Y(x)e^{i\phi}|)} \right| dx \tag{B4}$$

for $\phi \in [0, 2\pi]$.

APPENDIX C: COMPARISON OF EIGENMODES AND TIME-STEPPING SIMULATIONS WITH FREE-FREE BOUNDARY CONDITIONS

In Fig. 22, we compare the eigenmodes to the time-stepping simulations for two cases of free-free membranes: $(R_1, T_0) = (10^1, 10^{0.1})$ [Figs. 22(a), 22(c) and 22(e)] and $(10^{1.5}, 10^{0.2})$ [Figs. 22(b), 22(d) and 22(f)] at $R_3 = 10^{1.5}$ in both cases. The comparison methods for fixed-free membranes (see Appendix B) are used again here. In Figs. 22(a) and 22(b), we see close agreement between the real and imaginary parts of the eigenmodes obtained from the two methods. In Figs. 22(c) and 22(d), a point of inflection occurs close to the midpoint of the membrane, and migrates closer to the
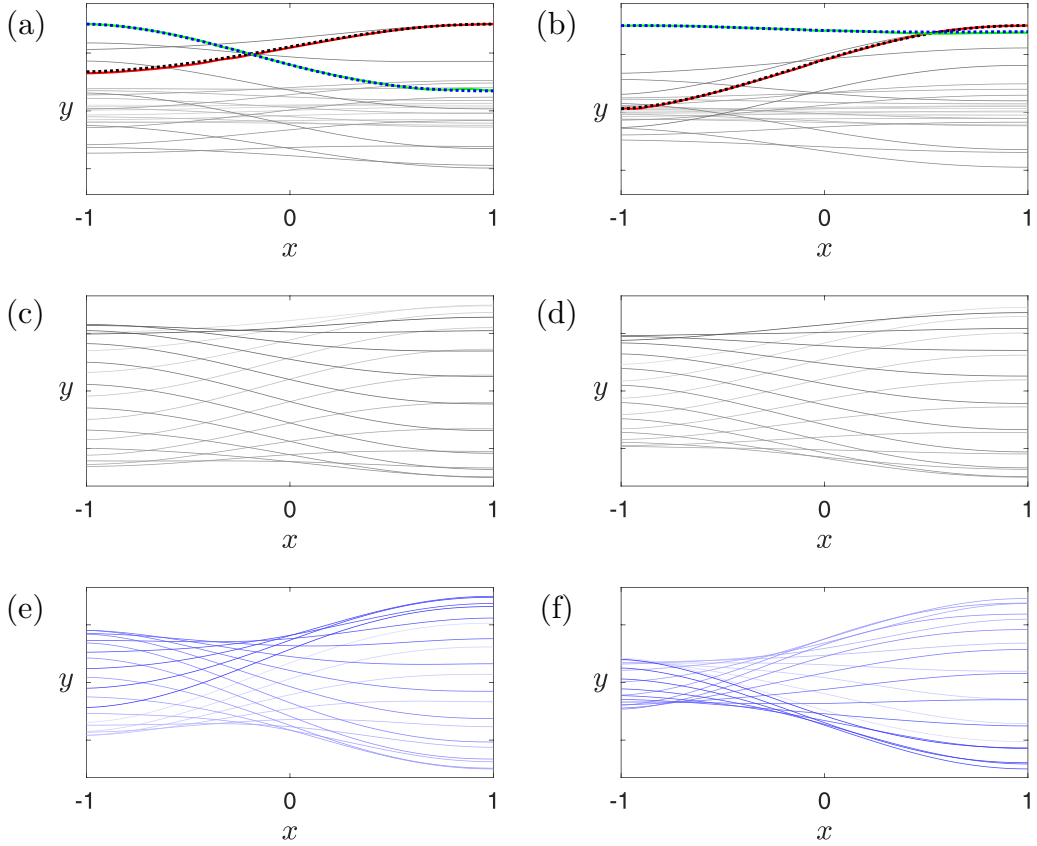
FIG. 22. Free-free membranes at $(R_1, T_0) = (10^1, 10^{0.1})$ for (a), (c), and (e) and at $(R_1, T_0) = (10^{1.5}, 10^{0.2})$ for (b), (d), and (f), with $R_3 = 10^{1.5}$ in both cases. These membranes lose stability by flutter and divergence. In (a) and (b), the solid red lines are $\mathrm{Re}(y_{\mathrm{ynonlin}}(\alpha))$ estimated from the time-stepping simulation, which are close to $\mathrm{Re}(Y(x))$ from the eigenvalue problem (dotted black lines). The solid green lines are $\mathrm{Im}(y_{\mathrm{ynonlin}}(\alpha))$, close to $\mathrm{Im}(Y(x))$ from the eigenvalue problem (dotted blue lines). The gray lines are a subset of snapshots in the linear growth regime. In (c) and (d), we show the snapshots during the small-amplitude (growth) regime but with the exponential growth removed. (e) and (f) show snapshots during the steady-state large-amplitude motions. Shades of gray (and blue) increase from light to dark as 20 membrane positions cycle through a period.

leading edge at large amplitude [Figs. 22(e) and 22(f)]. The small- and large-amplitude shapes are similar in terms of the number of local maxima and minima of deflection (typically one of each).

[1] C. Mavroyiakoumou and S. Alben, Large-amplitude membrane flutter in inviscid flow, J. Fluid Mech. **891**, A23 (2020).

[2] R. Sygulski, Stability of membrane in low subsonic flow, Inter. J. Non-Lin. Mech. **42**, 196 (2007).

[3] S. Tiomkin and D. E. Raveh, On the stability of two-dimensional membrane wings, J. Fluids Struct. **71**, 143 (2017).

[4] S. Colgate, *Fundamentals of Sailing, Cruising, and Racing* (WW Norton & Company, New York, 1996).

[5] J. Kimball, *Physics of Sailing* (CRC Press, Boca Raton, FL, 2009).

[6] B. G. Newman, Aerodynamic theory for membranes and sails, Prog. Aerosp. Sci. **24**, 1 (1987).

[7] B. G. Newman and H. T. Low, Two-dimensional impervious sails: Experimental results compared with theory, J. Fluid Mech. **144**, 445 (1984).

[8] J. N. Nielsen, Theory of flexible aerodynamic surfaces, J. Appl. Mech. **30**, 435 (1963).

[9] W. B. Pepper and R. C. Maydew, Aerodynamic decelerators-an engineering review, J. Aircr. **8**, 3 (1971).

[10] K. Stein, R. Benney, V. Kalro, T. E. Tezduyar, J. Leonard, and M. Accorsi, Parachute fluid–structure interactions: 3-D computation, Comput. Methods Appl. Mech. Eng. **190**, 373 (2000).

[11] R. Albertani, B. Stanford, J. P. Hubner, and P. G. Ifju, Aerodynamic coefficients and deformation measurements on flexible micro air vehicle wings, Exp. Mech. **47**, 625 (2007).

[12] H. Hu, M. Tamai, and J. T. Murphy, Flexible-membrane airfoils at low Reynolds numbers, J. Aircr. **45**, 1767 (2008).

[13] Y. Lian, W. Shyy, D. Viieru, and B. Zhang, Membrane wing aerodynamics for micro air vehicles, Prog. Aerosp. Sci. **39**, 425 (2003).

[14] W. Shyy, M. Berg, and D. Ljungqvist, Flapping and flexible wings for biological and micro air vehicles, Prog. Aerosp. Sci. **35**, 455 (1999).

[15] B. Stanford, P. Ifju, R. Albertani, and W. Shyy, Fixed membrane wings for micro air vehicles: Experimental characterization, numerical modeling, and tailoring, Prog. Aerosp. Sci. **44**, 258 (2008).

[16] R. R. Rohrschneider and R. D. Braun, Survey of ballute technology for aerocapture, J. Spacecr. Rockets **44**, 10 (2007).

[17] R. Scott, R. Bartels, and O. Kandil, An aeroelastic analysis of a thin flexible membrane, in *48th AIAA/ASME/ASCE/AHS/ASC Structures, Structural Dynamics, and Materials Conference* (Honolulu, Hawaii, 2007), p. 2316.

[18] H. Ashley and G. Zartarian, Piston theory-a new aerodynamic tool for the aeroelastician, J. Aeronaut. Sci. **23**, 1109 (1956).

[19] J. W. Miles, On the aerodynamic instability of thin panels, J. Aeronaut. Sci. **23**, 771 (1956).

[20] H. M. Voss, The effect of an external supersonic flow on the vibration characteristics of thin cylindrical shells, J. Aerosp. Sci. **28**, 945 (1961).

[21] K. Haruo, Flutter of hanging roofs and curved membrane roofs, Int. J. Solids Struct. **11**, 477 (1975).

[22] W. C. Knudson, Recent advances in the field of long span tension structures, Eng. Struct. **13**, 164 (1991).

[23] R. Sygulski, Dynamic stability of pneumatic structures in wind: Theory and experiment, J. Fluids Struct. **10**, 945 (1996).

[24] J. A. Cheney, N. Konow, A. Bearnot, and S. M. Swartz, A wrinkle in flight: The role of elastin fibres in the mechanical behavior of bat wing membranes, J. R. Soc., Interface **12**, 20141286 (2015).

[25] A. Song, X. Tian, E. Israeli, R. Galvao, K. Bishop, S. Swartz, and K. Breuer, Aeromechanics of membrane wings with implications for animal flight, AIAA J. **46**, 2096 (2008).

[26] S. M. Swartz, M. S. Groves, H. D. Kim, and W. R. Walsh, Mechanical properties of bat wing membrane skin, J. Zool. **239**, 357 (1996).

[27] E. H. Dowell and C. S. Ventres, Flutter of low aspect ratio plates, AIAA J. **8**, 1162 (1970).

[28] D. J. Johns, Supersonic membrane flutter, AIAA J. **9**, 960 (1971).

[29] J. H. Spriggs, A. F. Messiter, and W. J. Anderson, Membrane flutter paradox-an explanation by singular-perturbation methods, AIAA J. **7**, 1704 (1969).

[30] E. H. Dowell, *Aeroelasticity of Plates and Shells* (Springer Science & Business Media, Springer Netherlands, 1974), Vol. 1.

[31] S. C. Gibbs IV and E. H. Dowell, Membrane paradox for solar sails, AIAA J. **52**, 2904 (2014).

[32] A. Manela and M. Weidenfeld, The 'hanging flag' problem: On the heaving motion of a thin filament in the limit of small flexural stiffness, J. Fluid Mech. **829**, 190 (2017).

[33] B. G. Newman and M. P. Paidoussis, The stability of two-dimensional membranes in streaming flow, J. Fluids Struct. **5**, 443 (1991).

[34] J. W. Jaworski and R. E. Gordnier, High-order simulations of low Reynolds number membrane airfoils under prescribed motion, J. Fluids and Struct. **31**, 49 (2012).

[35] M. Nardini, S. J. Illingworth, and R. D. Sandberg, Reduced-order modeling for fluid-structure interaction of membrane wings at low and moderate Reynolds numbers, in *2018 AIAA Aerospace Sciences Meeting* (Kissimmee, Florida, 2018), p. 1544.

[36] O. Le Maître, S. Huberson, and E. S. De Cursi, Unsteady model of sail and flow interaction, J. Fluids Struct. **13**, 37 (1999).

[37] S. Alben, The flapping-flag instability as a nonlinear eigenvalue problem, Phys. Fluids **20**, 104106 (2008).

[38] P. Rojratsirikul, Z. Wang, and I. Gursul, Unsteady fluid-structure interactions of membrane airfoils at low Reynolds numbers, in *Animal Locomotion* (Springer, Berlin, Heidelberg, 2010), pp. 297–310.

[39] S. J. Farlow, *Partial Differential Equations for Scientists and Engineers* (Courier Corporation, New York, 1993).

[40] K. F. Graff, *Wave Motion in Elastic Solids* (Oxford University Press, Oxford, England, 1975).

[41] S. Alben and M. J. Shelley, Flapping States of a Flag in an Inviscid Fluid: Bistability and the Transition to Chaos, Phys. Rev. Lett. **100**, 074301 (2008).

[42] J. Allen, A. Techet, R. Kelso, and A. Smits, Energy harvesting eel, In 14th Australasian Fluid Mechanics Conference (Adelaide University, South Australia, 2001).

[43] M. Argentina and L. Mahadevan, Fluid-flow-induced flutter of a flag, Proc. Natl. Acad. Sci. USA **102**, 1829 (2005).

[44] B. S. H. Connell and D. K. P. Yue, Flapping dynamics of a flag in a uniform stream, J. Fluid Mech. **581**, 33 (2007).

[45] E. de Langre, M. P. Païdoussis, O. Doaré, and Y. Modarres-Sadeghi, Flutter of long flexible cylinders in axial flow, J. Fluid Mech. **571**, 371 (2007).

[46] C. Eloy, R. Lagrange, C. Souilliez, and L. Schouveiler, Aeroelastic instability of cantilevered flexible plates in uniform flow, J. Fluid Mech. **611**, 97 (2008).

[47] A. Goza, T. Colonius, and J. E. Sader, Global modes and nonlinear analysis of inverted-flag flapping, J. Fluid Mech. **857**, 312 (2018).

[48] W.-X. Huang, S. J. Shin, and H. J. Sung, Simulation of flexible filaments in a uniform flow by the immersed boundary method, J. Comput. Phys. **226**, 2206 (2007).

[49] L.-B. Jia, F. Li, X.-Z. Yin, and X.-Y. Yin, Coupling modes between two flapping filaments, J. Fluid Mech. **581**, 199 (2007).

[50] Y. Jin, K. Jin-Tae, S. Fu, and L. P. Chamorro, Flow-induced motions of flexible plates: Fluttering, twisting and orbital modes, J. Fluid Mech. **864**, 273 (2019).

[51] D. Kim, J. Cossé, C. H. Cerdeira, and M. Gharib, Flapping dynamics of an inverted flag, J. Fluid Mech., **736** (2013).

[52] A. Kornecki, E. H. Dowell, and J. O'Brien, On the aeroelastic instability of two-dimensional panels in uniform incompressible flow, J. Sound Vib. **47**, 163 (1976).

[53] A. Manela and M. S. Howe, On the stability and sound of an unforced flag, J. Sound Vib. **321**, 994 (2009).

[54] S. Michelin, S. G. Llewellyn Smith, and B. J. Glover, Vortex shedding model of a flapping flag, J. Fluid Mech. **617**, 1 (2008).

[55] J. Mougel, O. Doaré, and S. Michelin, Synchronized flutter of two slender flags, J. Fluid Mech. **801**, 652 (2016).

[56] S. Orrego, K. Shoele, A. Ruas, K. Doran, B. Caggiano, R. Mittal, and S. H. Kang, Harvesting ambient wind energy with an inverted piezoelectric flag, Appl. Energy **194**, 212 (2017).

[57] M. J. Shelley, N. Vandenberghe, and J. Zhang, Heavy Flags Undergo Spontaneous Oscillations in Flowing Water, Phys. Rev. Lett. **94**, 094302 (2005).

[58] D. M. Tang, H. Yamamoto, and E. H. Dowell, Flutter and limit cycle oscillations of two-dimensional panels in three-dimensional axial flow, J. Fluids Struct. **17**, 225 (2003).

[59] L. P. Tosi and T. Colonius, Modeling and simulation of a fluttering cantilever in channel flow, J. Fluids Struct. **89**, 174 (2019).

[60] L. Zhu and C. S. Peskin, Simulation of a flapping flexible filament in a flowing soap film by the immersed boundary method, J. Comput. Phys. **179**, 452 (2002).

[61] S. Arbós-Torrent, B. Ganapathisubramani, and R. Palacios, Leading-and trailing-edge effects on the aeromechanics of membrane aerofoils, J. Fluids Struct. **38**, 107 (2013).

[62] M. R. Sunny, C. Sultan, and R. K. Kapania, Optimal energy harvesting from a membrane attached to a tensegrity structure, AIAA J. **52**, 307 (2014).

[63] S. Yang and C. Sultan, Modeling of tensegrity-membrane systems, Int. J. Solids Struct. **82**, 125 (2016).

[64] M. S. Triantafyllou and C. T. Howell, Dynamic response of cables under negative tension: An ill-posed problem, J. Sound Vib. **173**, 433 (1994).

[65] M. J. Shelley and J. Zhang, Flapping and bending bodies interacting with fluid flows, Annu. Rev. Fluid Mech. **43**, 449 (2011).

[66] E. Kashy, D. A. Johnson, J. McIntyre, and S. L. Wolfe, Transverse standing waves in a string with free ends, Am. J. Phys. **65**, 310 (1997).

[67] G. F. Carrier, On the non-linear vibration problem of the elastic string, Q. Appl. Math. **3**, 157 (1945).

[68] R. Narasimha, Non-linear vibration of an elastic string, J. Sound Vib. **8**, 134 (1968).

[69] A. H. Nayfeh and P. F. Pai, *Linear and Nonlinear Structural Mechanics* (John Wiley & Sons, New York, 2008).

[70] A. Ralston and P. Rabinowitz, *A First Course in Numerical Analysis* (Courier Corporation, Mineola, New York, 2001).